# Density Functional Theory Study of the Partial Oxidation of Methane to Methanol on Au and Pd Surfaces

Ali Nasrallah[1], Julien Engel[1], C. Richard A. Catlow[1,2] and David J. Willock[1*]

(1) School of Chemistry, Cardiff University, Main Building, Park Place, CF10 3AT, Cardiff, United Kingdom
(2) Department of Chemistry, University College London, 20 Gordon St., London WC1 HOAJ

**Abstract**

The partial oxidation of methane to methanol has been a goal of heterogeneous catalysis for many years. Recent experimental investigations have shown how AuPd nanoparticle catalysts can give good selectivity to methanol with only limited total oxidation of $CH_4$ using hydrogen peroxide as an oxidant in aqueous media. Interestingly, the use of colloidal nanoparticles alone, without a support material, leads to efficient use of the oxidant and the possibility of introducing oxygen from $O_2$(g) into the $CH_3O_2H$ primary product. This observation indicates that a radical mechanism is being initiated by $H_2O_2$ but then the oxygen addition step, catalysed by these nanoparticles, can incorporate $O_2$(ads). In this contribution, we use Density Functional Theory (DFT) to study the elementary steps in the partial oxidation of methane to methanol using $H_2O_2$ as a radical initiator and molecular oxygen as oxidant over the low index surfaces of Pd and Au. We are able to show that pure Pd nanoparticles are prone to oxidation by $O_2$(g) whereas the competitive adsorption of water on Au surfaces limits the availability of $O_2$(ads). Calculations with Au added to Pd or *visa versa* show that both effects can be alleviated by using mixed metal surfaces. This provides a rationalization of the need to use alloy nanoparticles experimentally and the insights from these results will aid future catalyst development.

## Introduction

Methane, as the main component of natural gas, finds wide spread use as a fuel in industry, the energy generation sector and domestic settings. The incorporation of methane into chemical synthesis, however, is more challenging. Currently this is only commercially possible via conversion to syngas (a mixture of $H_2$ and CO) and then upgrading to higher molecular weight products via the Fischer Tropsch synthesis,[1] and methane coupling technologies.[2] The energy demands for these indirect routes are high,[3] requiring temperatures in excess of 1000 K and so are usually carried out on a large scale, which makes these approaches unsuitable for the remote locations and distributed nature of current natural gas reserves. Transportation of methane is also costly due to its low boiling point ( -164 °C ) so that gas pipe lines or cryogenically cooled tankers are required to transfer the gas to processing plants. Renewable sources of methane, such as the methane generated by anerobic waste decomposition on land fill sites and methane produced as a way to valorize excess renewable energy are also becoming available,[4] meaning that technologies developed to process methane will be useful as a more sustainable chemical economy is developed. The capture and utilization of methane from land fill sites and other anthropogenic sources of methane is also important as part of a strategy to reduce global temperature rises. Methane is the second highest contributor to the greenhouse effect after $CO_2$, and is responsible for around 20% of the warming induced by long-lived greenhouse gases emitted in to the atmosphere since industrialization.[5] Accordingly, there is great interest in developing a low temperature route for the direct partial oxidation of methane to methanol, formaldehyde or formic acid so that liquid transportation becomes possible and direct use in technologies such as fuel cell generators can be enabled.[6] In particular, direct partial oxidation of methane to methanol has attracted much attention, as methanol is used as a feedstock for the production of important chemicals such as dimethyl ether,[7,8] formaldehyde,[9] and propylene.[10]

The partial oxidation of methane is challenging: methane is a non-polar molecule with a C-H bond energy of 439 kJ $mol^{-1}$ making the activation of the molecule difficult.[11] In addition, while the enthalpy of reaction to form methanol with dioxygen is favourable ( $\Delta H^{\Theta}_{298\ K}$ = -126 kJ $mol^{-1}$ ), the C-H bond strength of methanol ( 402 kJ $mol^{-1}$ ) is lower than that of methane, so that further oxidation is likely to occur under conditions in which methane is activated. Early work in the

heterogeneously catalysed direct partial oxidation of methane concentrated on high temperature gas phase chemistry using transition metal oxide catalysts such as molybdenum and vanadium oxide.[12,13,14,15] These reactions relied on the activation of methane by lattice oxide species and the subsequent redox cycling of the metal cations.[16] However, at the temperatures used (400 °C) gas phase radical chemistry and the competition of complete oxidation limits the selectivity to partial oxygenates.

Cu/Fe zeolites with $N_2O$ or $O_2$ (for Cu) as the oxidant have also been used for the partial oxidation of methane to form methanol.[17] In the case of Fe-ZSM-5 the mechanism involves a highly reactive α-oxygen species ($Fe^{III}$-$O^{-}$•) which is set up by reaction of $N_2O$ with the extra-framework $Fe^{II}$ cation sites at 200-250 °C. Methane is then reacted with the pre-prepared zeolite at room temperature and methanol obtained using an extraction step.[18] In the case of Cu the extra-framework species is also a highly reactive oxygen radical anion species formed at a bridge site between two extra-framework cations $Cu^{II}$-$O^{-}$•-$Cu^{I}$.[19] For Cu-ZSM-5, the reactive oxygen can be prepared from $O_2$(g) at temperatures < 200 °C. Passing methane over the pre-prepared material at lower temperatures (100 – 200 °C) then generates methanol precursors that can be extracted from the zeolite by extraction with a suitable solvent. During the activation of methane in these systems, a strong O-H bond to the oxygen radical anion is formed providing the energy required to break the $H_3C$-H bond. However, the processes are not catalytic as the preparation of the oxygen radical anion is carried out under different conditions to the oxidation of methane.[20] The process also results in methoxy species bound to the zeolite framework that have to be solvent extracted to produce methanol. Fe-ZSM-5 has produced catalytic reactions when used with aqueous $H_2O_2$ as oxidant. However, the proposed catalytic cycle requires two moles of $H_2O_2$ for each mole of methanol produced.[21] The first is to set up the highly oxidised metal centre and the second to produce the methyl hydroperoxide seen as the primary oxidation product.

At the same time as high temperature methane oxidation routes were being explored in heterogeneous catalysis, models for the decomposition of atmospheric methane demonstrated that the energy demand of methane activation could be achieved through reaction with •OH radical species.[22] These radicals are generated when singlet atomic oxygen ($O(^1D)$) derived from the photochemical decomposition of ozone interact with atmospheric water vapour. The methyl radicals produced in this process go on to react with molecular oxygen to form methyl peroxy

radicals ($CH_3O_2$•) in the initiation of the oxidation process that ultimately acts to decompose atmospheric methane.[22]

Partial oxidation of methane with supported AuPd catalysts using $H_2O_2$ as the oxidant are also thought to operate through methane activation by the •OH radicals generated from $H_2O_2$ decomposition. Studies by Ab Rahim *et al.* reported the partial oxidation of methane using supported Au-Pd nanoparticles under mild condition with $H_2O_2$ as an oxidant at 50 °C.[23] Using electron paramagnetic resonance (EPR) spectroscopy, they were able to detect the presence of both methyl (•$CH_3$) and hydroxyl (•OH) radicals.

However, due to the relatively high cost of hydrogen peroxide compared to the current market price of methanol, it is unlikely that using hydrogen peroxide as oxidant will be lead to an industrial method of generating methanol. The most cost effective oxidant would be $O_2$(g) but usually reaction of hydrocarbons with dioxygen favour total oxidation to $CO_2$. Agarwal *et al.* investigated the incorporation of molecular oxygen into the AuPd nanoparticle catalysed reaction in combination with $H_2O_2$ using colloidal Au-Pd nanoparticles at 50 °C.[24] Their work highlighted the superior activity of the colloidal alloy to both the titania-supported alloy and the pure metal colloids. Au-Pd nanoparticles supported on titania exhibit a high rate of hydrogen peroxide degradation. The colloidal alloy on the other hand, showed lower $H_2O_2$ decomposition and exhibited substantially higher product yields compared to the supported catalyst. The addition of 5 bar of molecular oxygen into the head space above the reaction mixture also showed an increase in the product yield from 15.7 μmol to 26.8 μmol while maintaining a high selectivity of 95% to partial oxygenates. In order to demonstrate that the source of oxygen in the methyl hydroperoxide is indeed molecular oxygen, isotopic labelling experiments were conducted by adding 5 bar of $^{18}O_2$ into the reaction mixture. Mass spectroscopy analysis of the primary products revealed that 51% of the observed signal corresponded to $CH_3OH$ mass fragments containing an $^{18}O$ label. Reactions in the absence of hydrogen peroxide, but in the presence of molecular oxygen showed no product formation indicating that the presence of hydrogen peroxide is crucial for the initiation step. Even so, levels of hydrogen peroxide as low as 500 μmol in the 10 ml reaction mixture resulted in an increase in the reaction products from 43 μmol with no gas phase oxygen to 50 μmol, when oxygen was included. This observation further supports the role played by hydrogen peroxide as only an initiator in the radical oxidation process. Pure Au and Pd showed only low activity for methane

oxidation further suggesting that the alloyed nanoparticles display a synergistic effect in terms of both catalyst stability and activity for the reaction. Scheme 1 shows a reaction mechanism that was put forward based on the AuPd colloidal catalyst results. Hydrogen peroxide is first activated to produce •OH radicals which in turn can abstract a hydrogen atom from methane. The methyl radicals generated can then react with the dissolved oxygen resulting in the incorporation of molecular oxygen into more than 70% of the primary products as demonstrated by $H_2{}^{16}O_2$ with

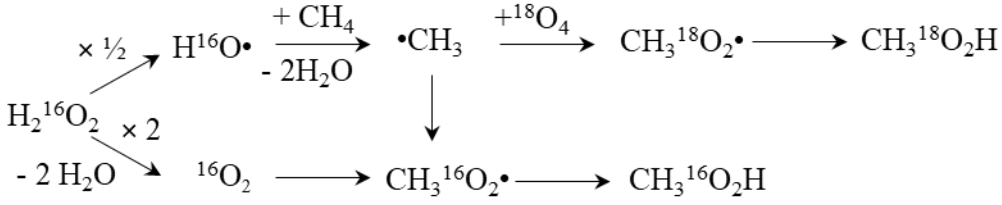


Scheme 1: Proposed reaction scheme of the partial oxidation of methane to methyl hydroperoxide using hydrogen peroxide and oxygen as oxidants.

$^{18}O_2$ experiments. Products containing $^{16}O$ were also formed, as a result of reaction of $•CH_3$ with either $•{}^{16}O{}^{16}OH$ or $^{16}O_2$ formed from the decomposition of hydrogen peroxide. This study demonstrated that once the $H_3C–H$ bond in methane is activated using hydrogen peroxide, it is possible to incorporate molecular oxygen in to the primary intermediate in this reaction: methyl hydroperoxide ($CH_3O_2H$, Scheme 1). Isotopic labelling experiments have shown that methyl hydroperoxide then reacts further over AuPd nanoparticles to produce methanol.[23] Converting methane to methanol with the incorporation of $O_2$(g) in this way would make the entire process substantially cheaper and more likely to be economically viable.

The oxidation of methane over Au/Pd catalysts has also been the subject of a number of theoretical studies. Weaver and co-authors have also considered alkane adsorption over Pd and PdO surfaces making a comparison of adsorption energy, $E_{ads}$, estimated from temperature programmed desorption experiments and dispersion corrected DFT (PBE+D3).[25] They find a linear relation between alkane chain length and adsorption energy with estimates for methane on Pd(111) of $E_{ads}$ = -16 kJ mol$^{-1}$ (Pd(111), TPD) *cf.* $E_{ads}$ = -24 kJ mol$^{-1}$ (Pd(111), PBE+D3).[26] In their calculations the contribution of dispersion to the adsorption energy is critical and PBE alone actually gives slightly unfavourable $E_{ads}$ values. Adsorption of methane to PdO(101) is found to be somewhat stronger, $E_{ads}$ = -42 kJ mol$^{-1}$ (PdO(101), TPD) *cf.* $E_{ads}$ = -41 kJ mol$^{-1}$ (PdO(101), PBE+D3). They explain this relatively strong interaction of saturated hydrocarbons with the oxide surface as

coming from a σ-complex formed by charge donation from the alkane to under co-ordinated $Pd^{2+}$ centres on the PdO(101) surface. This also acts as a precursor to $H_3C$-H bond cleavage.[27] Very recently, Yoshizawa and co-workers[28] have used periodic DFT with the PBE functional to study methane activation and oxidation with $H_2O_2$ over Pd(111) and a Pd(111) surface modified by the inclusion of a single Au atom in the surface. They find that the activation of methane by reaction with surface bound OH(ads) species generated on decomposition of hydrogen peroxide is an effective route to activating methane with a side product of water. They then consider the formation of methanol directly from the methyl radical and OH(ads) and find that this is the rate determining step for methanol production via this reaction profile. The inclusion of Au in the surface of Pd(111) slab model also lead to a significantly weaker interaction between OH(ads) and the surface leading to a further reduction of the barrier for methane activation compared the pure Pd(111) surface.

The aim of this work is to use dispersion corrected density functional theory (DFT) calculations to consider the elementary steps that underpin the reactions in Scheme 1, with methanol being produced via the methyl hydroperoxide intermediate observed experimentally and consider the production of this intermediate via $H_3C$-$O_2$ bond formation between surface bound methyl radicals and co-adsorbed molecular oxygen. We concentrate on the surfaces of Au and Pd as pure metal catalysts to map out the whole scheme and highlight key steps which limit their activity for methane partial oxidation. We then analyse these points more closely by making single atom substitutions[28] ( Au into Pd and Pd into Au ) to understand how alloying is able to increase the efficacy of the colloidal catalysts compared to the pure metal systems. Structural examination of the AuPd alloy colloids has revealed that the nanoparticles produced experimentally have mostly icosahedral structures with some cuboctahedral characteristics.[29] Accordingly, we model the (111) and the (100) surface facets of Au and Pd.

**Computational Details**

All calculations presented employ Density Functional Theory (DFT) as implemented within the VASP (Vienna Ab initio Software Package) code.[30,31,32,33] The Perdew-Burke-Ernzerhof (PBE) exchange-correlation functional[34,35] is employed to account for the exchange and correlation effects with the projector augmented-wave (PAW) method to represent core states.[36,37] Previous work has shown that the use of the PBE functional to study the interaction of organic compounds

on transition metal surfaces gives a good representative of adsorption energies and transition states.[38,39, 40,41]

The energy cut off for the plane wave basis set and the electronic self-consistent field (SCF) threshold were set to 400 eV and $10^{-4}$ eV respectively. Calculations were also set to converge when the forces are less than 0.01 eV $Å^{-1}$ for adsorption calculations and 0.001 eV $Å^{-1}$ for bulk and surface optimisation calculations. A Monkhorst-Pack grid was used to sample the Brillouin zone[42]. For optimisation calculations, the number of *k*-points used was 7×7×7 for the bulk, and 7×7×1 for the surfaces. For the adsorption calculations, we employed supercell expansions and so it was possible to lower *k*-point sampling to 3×3×1. Dispersion corrections were included to account for van der Waals interactions using Grimme's empirical DFT -D3 model.[43]

To create surface models 5-layered (111) and (100) slabs were cut from the optimised bulk. In each of the surfaces, the bottom three layers were fixed with the top two layers free to move. In order to avoid interactions between the periodically repeated slabs, a vacuum layer of 13 Å was introduced above the surface. The number of atoms in the (111) surfaces was set to 80 atoms to give 16 atoms in the surface layer in a *p*(4×4) arrangement (figure S1*a*). For the (100) surfaces, two different slab sizes were used. Slabs containing 40-atoms were used to assess surface relaxation, calculate the surface energy of the clean surface and carry out adsorption and dissociation barrier calculations for single molecule steps in the reaction scheme. Larger 90-atom slabs were needed in order to avoid interactions between the adsorbates in the surface vector directions when more than one molecule is involved in an elementary step. In both cases a square 2-D surface repeat unit was used (figure S1*b*). The 90-atom slab was used to model the hydrogen abstraction from methane, the formation of the methyl peroxy intermediate, the activation of methane by an oxygen species, and calculations on the mixed metal surfaces. Dipole correction along the *z*-direction of the slab was also applied in all calculations. The parameters used in the calculations were benchmarked against the convergence of the surface energy as described in the supplementary information section S1. In particular, the inclusion of dispersion corrections was found to lead to a significant increase in the calculated surface energy for all surfaces (compare converged values in Tables S1 and S2). The values with dispersion included are in good agreement with experimental estimates (1.5 J $m^{-2}$ for Au and 2.0 J $m^{-2}$ for Pd).[44]

The energy of adsorption was calculated as:

$$E_{ads} = (E_{ad+sl} - E_{sl} - E_{ad}) \quad (1)$$

Where $E_{ad+sl}$ is the electronic energy of the adsorbed structure, $E_{sl}$ is the energy of the reference optimised slab, and $E_{ad}$ is the energy of the adsorbate in gas phase.

The key energetic information for each elementary step can also be derived from these adsorption energies. For example, the barrier for a particular step is given by:

$$E_b = E_{ads}(TS) - E_{ads}(R) \quad (2)$$

where $E_{ads}$(TS) is the adsorption energy calculated for the transition state structure and $E_{ads}$(R) is the adsorption energy calculated for the reactant state of that elementary step. Similarly the overall change of system energy over an elementary step, $\Delta E$, can be informative. For example, the dissociation energy of a molecular species would be obtained from:

$$\Delta E_{diss} = E_{ads}(P) - E_{ads}(R) \quad (3)$$

Where $\mathrm{E_{ads}}$(P) is the adsorption energy for the product state, *i.e.* the dissociated state of the molecule.

To find transition states, initial guesses identified from optimised structures using the nudged elastic band (NEB)[45] approach were further refined with the dimer method[46] and checked as true saddle points using frequency calculations. A transition state was confirmed when the calculated gradient on all atoms was lower than the geometry optimisation criteria and the calculated frequencies contained a single negative mode indicating an imaginary force constant along the reaction coordinate. The motion along the eigenvector of the negative mode was visualised to confirm that it corresponded to the expected bond breaking/forming process.

It is usually possible for the adsorbate on a surface to have more than one configuration with the lowest energy configuration expected to have the greatest population. Our nomenclature defines the possible configurations with respect to the position of the atoms of the adsorbate relative to the nearest metal atoms, as defined in figure 1*a* using the example of Pd(111). For the (111) surface the positions are top, bridge, hcp-hollow and fcc-hollow, we use the same nomenclature for (100) surfaces but the distinction of fcc and hcp hollow sites is not required. When molecular species are adsorbed the configuration can be more complex as the orientation of the molecule relative to the surface has to be taken into account. For molecules we will refer to the positions of the atoms

interacting with the surface, for example, figure 1*b* shows a methyl peroxide species in a hollow-bridge configuration on the Au(100) surface.

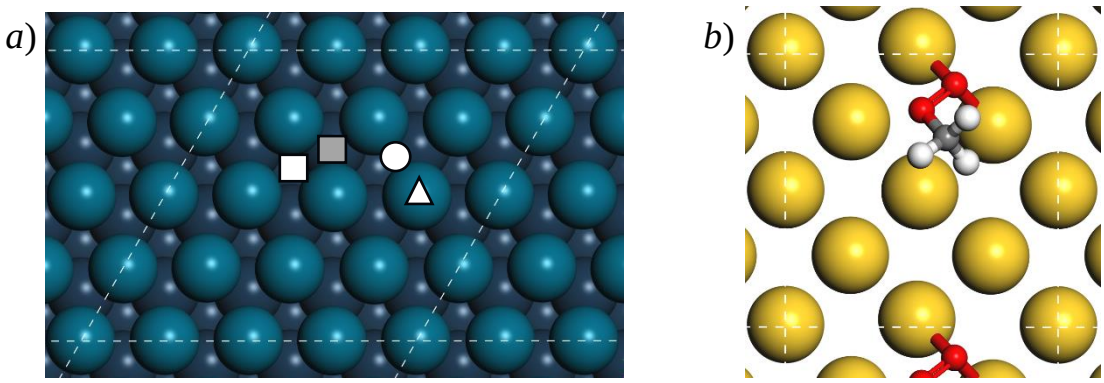


Figure 1: *a*) The position of the atoms in top (triangle), bridge (circle), and hollow (rectangle/ grey rectangle) configurations *b*) Example of a hollow-bridge configuration on the Au(100) surface. Atom colours: Au; yellow, Pd; blue, C; grey, O; red and H; white.

Bader analysis[47] as implemented by Henkleman and co-workers[48,49,50] was used to obtain the atomic charges for some of the optimised structures in this study. The atomic charges are derived from integration over atomic basins using the charge density represented on a regular three dimensional grid. Table S3 shows that a grid spacing of 0.02 Å is sufficient to obtain charges converged to $10^{-3}$ |e| which allows values to be quoted to three decimal places in our discussion of results.

**Results and Discussion**

Scheme 2 shows the proposed elementary steps in the oxidation of methane to methanol using initiation with $H_2O_2$ and oxygen incorporation from $O_2$. The process is split into three main sections: (i) The initiation reaction *i.e.* the activation of hydrogen peroxide (**1**) and the formation of surface bound hydroxyl radicals (**2**). (ii) The catalytic cycle, involving the activation of methane by •OH(ads) to form a surface •$CH_3$(ads) radical (**2**→**3**) and water, adsorption of oxygen and the desorption of water (**3**→**4**) followed by the reaction of •$CH_3$(ads) and $O_2$(ads) to form methyl peroxide (**4**→**5**) which is protonated by water to form the primary intermediate, methyl hydroperoxide and restore the starting point of the cycle (**5**→**6,2**). (iii) The cleavage of the $CH_3O$-OH bond in methyl hydroperoxide (**6**→**7**) and proton transfer to form a surface O atom and methanol (**7**→**8**).

The DFT calculated energies and structures for each elementary step in this scheme have been obtained for the (111) and (100) surfaces of Au and Pd and are described in the following sections. The resulting potential energy profile for the scheme is then used to discuss the implications for the overall process.

**i) Initiation: Adsorption and cleavage of hydrogen peroxide on the surface**

Table 1 summarises the adsorption energy of hydrogen peroxide on the different surfaces and the M—O distances from the optimised structures (M = Au or Pd). The corresponding relaxed structures are shown in Figure S2. In all cases $H_2O_2$ adsorbs molecularly in a top-hollow configuration. The hydrogen atom bonded to the oxygen atom in the hollow position was also found to be towards the surface so that the oxygen atom at this position does not directly interact with metal atoms. To test if this orientation of the hydrogen atom was a result of the dispersion correction included in our calculations the structure of the Pd(100)/$H_2O_2$ example was re-optimised without the dispersion parameters but no change in the configuration of the molecule on

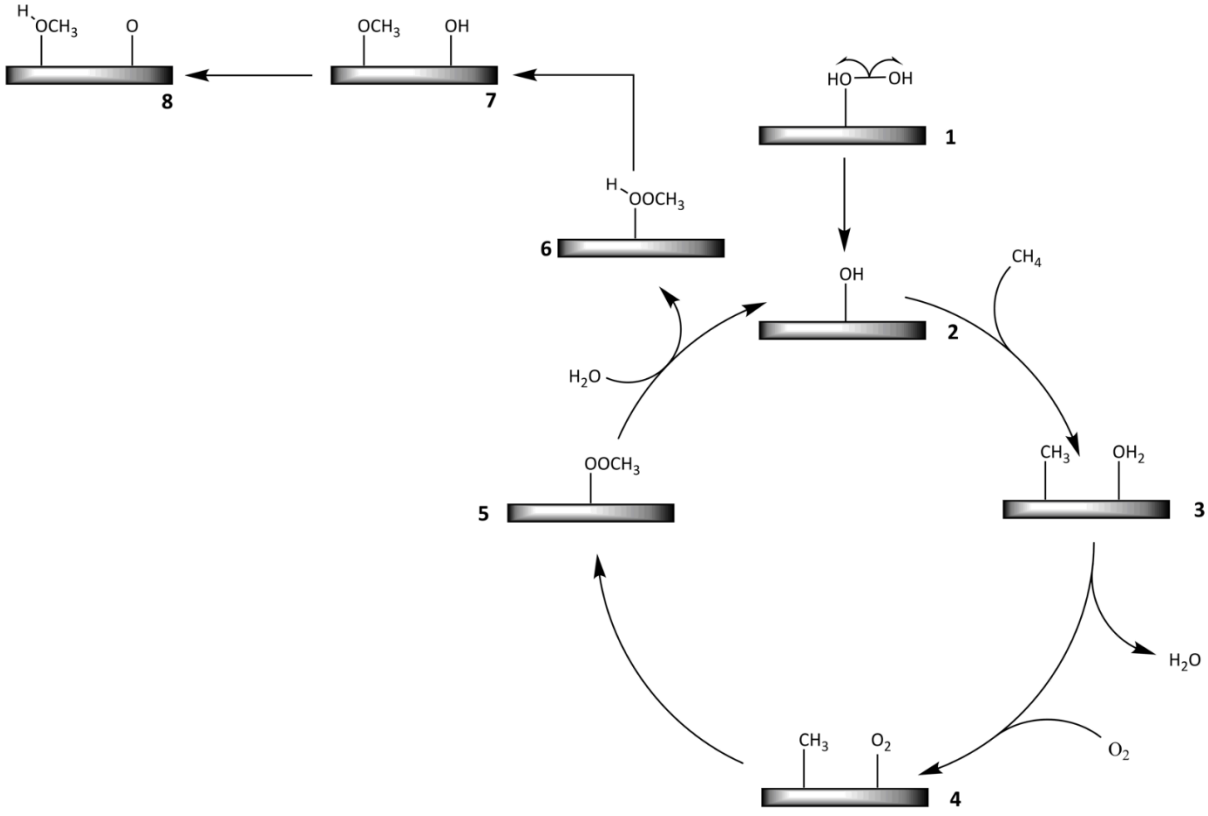


Scheme 2: The proposed mechanism for the catalytic formation of methanol on a metal nanoparticle surface.

the surface was observed beyond small changes in the inter-atomic distances. Using our standard approach, the molecular adsorption energies for hydrogen peroxide on the Pd surfaces are around 15 kJ mol$^{-1}$ more negative than those on the corresponding Au surfaces. For both metals, there is also a slightly more favourable adsorption energy on the (100) surface compared to the (111), by 2 kJ mol$^{-1}$ for Au and by only 1 kJ mol$^{-1}$ for Pd. The estimated van der Waals radius for Au is 0.30 Å greater than that of Pd ( Au: 2.45 Å, Pd: 2.15 Å )[51] and so the shorter M..(H)OOH distance for the oxygen at the top site seen here for the Pd surfaces is not unexpected, but is still consistent with the stronger interaction of $H_2O_2$ with Pd compared to that for Au that is indicated by the $E_{ads}$ data.

Starting structures for adsorbed $H_2O_2$ in the dissociated state on each surface were obtained by extending the HO-OH bond of the molecularly adsorbed system and then optimising the resulting structure to produce two surface OH(ads) groups. Figure 2 shows the calculated energy profiles for the dissociation process for each surface and energetic and structural information is also included in Table 1. In all of the configurations tested, both hydroxyl radicals relax to bridge

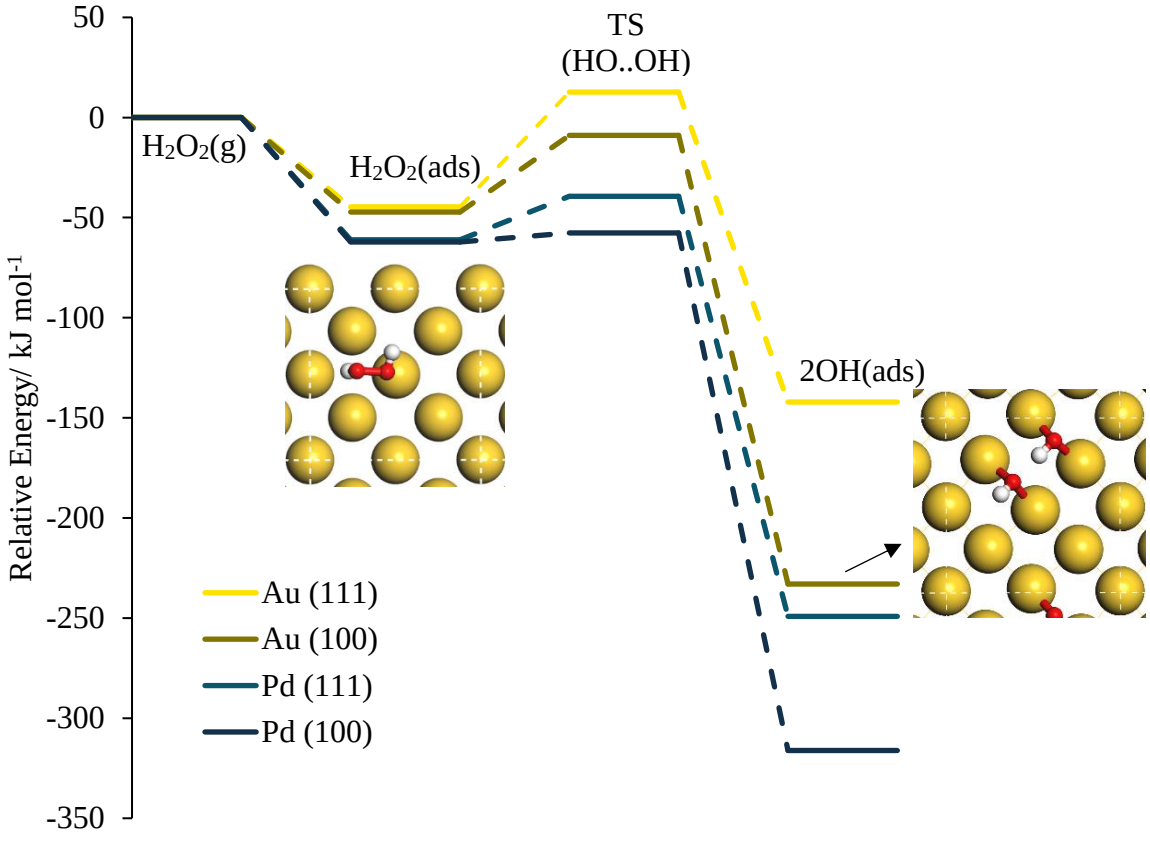


Figure 2: The calculated potential energy diagram for the adsorption and dissociation of $H_2O_2$ over Au(111) (yellow), Au(100) (orange), Pd(111) (blue) and Pd(100) (purple). TS: transition state for the dissociation step. Atom colours on inset images: Au; yellow, Pd; blue, C; grey, O; red and H; white.

positions. The most stable configurations were also found to have the OH(ads) species interacting via a hydrogen bond with a short OH..OH distance of between 1.75 Å and 1.93 Å (Table 1) as shown in figure 2 (inset right).

The Bader charge analysis for all surfaces is summarised in Table S4. It indicates that there is charge transfer between the surface and •OH(ads) of between -0.345 |*e*| and -0.482 |*e*| with the •OH(ads) acting as hydrogen bond donor showing the more negative charge in each case. A reference calculation of the bulk structure of $Mg(OH)_2$ yields a Bader charge for $OH^-$ of -0.875 |*e*| and so we conclude that, on these metallic surfaces, the •OH(ads) species is better described as a surface stabilised radical than as a hydroxyl group.

The energies of the molecularly adsorbed structures, the barrier to dissociation (equation 2) and the dissociation energy (using equation 3) are also given in Table 1. For both Pd and Au surfaces, the dissociation reaction is exothermic and the two hydroxyl radicals are more stabilised by the (100) surface than by the (111) surface, by around 66 kJ $mol^{-1}$ for Pd and by 88 kJ $mol^{-1}$ for Au. This may be due to surface geometry which can accommodate a shorter hydrogen bond interaction on the (100) surface compared to the (111), by 0.05 Å in the case of Au and by 0.18 Å for Pd. We also note that the two hydroxyl radicals bind more strongly to the Pd surfaces than to the Au

Table 1: The adsorption of hydrogen peroxide on the (111) and (100) surfaces of Au and Pd.

| **Surface** | $E_{ads}$[a] **/ kJ mol$^{-1}$** | **M..(H)OOH[b] / Å** | $E_b$[c] **/ kJ mol$^{-1}$** | $\Delta E_{dis}$[e] **/ kJ mol$^{-1}$** | **M—OH[f] / Å** | **OH…O(H) / Å** |
|---|---|---|---|---|---|---|
| Au (111) | -45 | 2.769 | 57 | -98 | 2.221-2.309 | 1.837 |
| Au (100) | -47 | 2.662 | 38 | -186 | 2.176-2.232 | 1.788 |
| Pd (111) | -61 | 2.342 | 5[d] | -188 | 2.112-2.172 | 1.933 |
| Pd (100) | -62 | 2.328 | 22[d] | -254 | 2.067-2.126 | 1.752 |

Note: *a*) Molecularly adsorbed state, *b*) distance for top site O in molecularly adsorbed state, M refers to either Au or Pd. *c*) Activation energy for HO-OH bond cleavage. *d*) Barrier involves rotation around HO-OH bond to move H out of hollow site. *e*) Dissociation energy taken as the difference between dissociated and molecularly adsorbed states. *f*) Average of bond lengths for the two OH groups formed on dissociation.

surfaces with the Pd(100) giving a dissociated adsorption energy of -316 kJ $mol^{-1}$ with reference to the gas phase $H_2O_2$ molecule.

The cleavage of hydrogen peroxide has higher barriers over Au surfaces than over Pd. The barriers for the cleavage of $H_2O_2$ on the Au(100) and Au(111) surfaces were found to be 38 kJ $mol^{-1}$ and 57 kJ $mol^{-1}$, respectively. Noting that the difference between the barriers for the surfaces is much smaller than that between the dissociation energies, $\Delta E_{dis}$, suggests that the barrier is early in the

reaction co-ordinate. Determination of the barriers for the cleavage of hydrogen peroxide on the Pd surfaces was more challenging. On both Pd surfaces, a rotation of the OH in the hollow position around the HO-OH bond to point the H atom away from the surface resulted in cleavage of the hydrogen peroxide to form two hydroxyl radicals. Accordingly, the activation energy for the hydrogen peroxide dissociation given in Table 1 corresponds to this rotation, which has a barrier of only 5 kJ $mol^{-1}$ on the Pd(111) surface and a barrier of 22 kJ $mol^{-1}$ on Pd (100). These results are in good agreement with the PBE level calculations reported by Li *et al*. who found a barrier of 2 kJ $mol^{-1}$ and estimate of $\Delta E_{dis}$=172 kJ $mol^{-1}$ for Pd(111).[52]

In summary, the dissociation of hydrogen peroxide through HO-OH cleavage ( **1**→**2** in Scheme 2) is an easy process to achieve with a strong thermodynamic driving force toward the product surface bound •OH(ads) species and low calculated barriers for all surfaces except Au(111). The Pd surfaces offer both lower barriers to this step and a higher affinity for the dissociated product than do the Au surfaces.

**ii) The Catalytic Cycle**

*Hydrogen abstraction from Methane*

Table 2: Calculated data for hydrogen abstraction from methane by hydroxyl radicals.

| **Surface** | $\Delta E_R$ [a] **/kJ mol$^{-1}$** | $E_b$ **/kJ mol$^{-1}$** | **M—OH** [b] **/Å** | **M—$CH_3$** [b] **/Å** | **M—$OH_2$** [b] **/Å** | $E_{ads}$**(OH)** [c] **/kJ mol$^{-1}$** | $E_{ads}$**($CH_3$)** [c] **/kJ mol$^{-1}$** |
|---|---|---|---|---|---|---|---|
| Au (111) | -36 | 87 | 2.269 | 2.120 | 2.961 | -203 | -148 |
| Pd (111) | -25 | 94 | 2.130 | 2.044 | 2.409 | -264 | -194 |
| Au (100) | +6 | 97 | 2.214 | 2.102 | 2.710 | -249 | -159 |
| Pd (100) | +6 | 88 | 2.095 | 2.033 | 2.451 | -306 | -200 |

Note: *a*) Reaction energy for $CH_4$(ads) + •OH(ads) = •$CH_3$(ads) + $H_2O$(ads), *b*) M corresponds to either Au or Pd. *c*) Adsorption energies refer to •OH(ads)/•$CH_3$(ads) relative to the corresponding gas phase species.

The first step in the catalytic cycle stage of the reaction mechanism laid out in Scheme 2 (**2**→**3**) involves the abstraction of hydrogen from methane by a hydroxyl radical. This step is considered to be the most energetically demanding in the conversion of methane to methanol due to the stability of the $H_3C$-H bond; the experimentally determined $H_3C$-H bond dissociation enthalpy at 298 K has a value of 439 kJ $mol^{-1}$.[53] The calculated energy profiles for each of the surfaces are shown in Figure 3 with key energy and geometric values given in Table 2. The calculations on the adsorption and dissociation of $H_2O_2$ have shown that the formation of surface bound hydroxyl

radical species is straight forward. Accordingly, for the catalytic cycle phase of the reaction we have taken a reference state of a single surface hydroxyl radical and isolated methane.

Configurations of physisorbed methane and the •OH(ads) species were optimised on the different surfaces. Following on from the hydrogen peroxide dissociation results, •OH(ads) was placed in a bridge position. The position of the methane molecule on the surface was initiated at a top position 3.0-3.5 Å away from the closest metal atom, however, on relaxation, the molecule usually moved to a neighbouring hollow site (*e.g.* Figure 3, inset left) with a closer interaction with the surface. The calculated adsorption energy of methane to the Pd(111)OH surface ( -26 kJ $mol^{-1}$ ) is in good agreement with the PBE+D3 results of Weaver and co-workers for clean Pd(111).[26] The orientation of the hydroxyl species with the hydrogen atom pointing away from the methane molecule was selected.

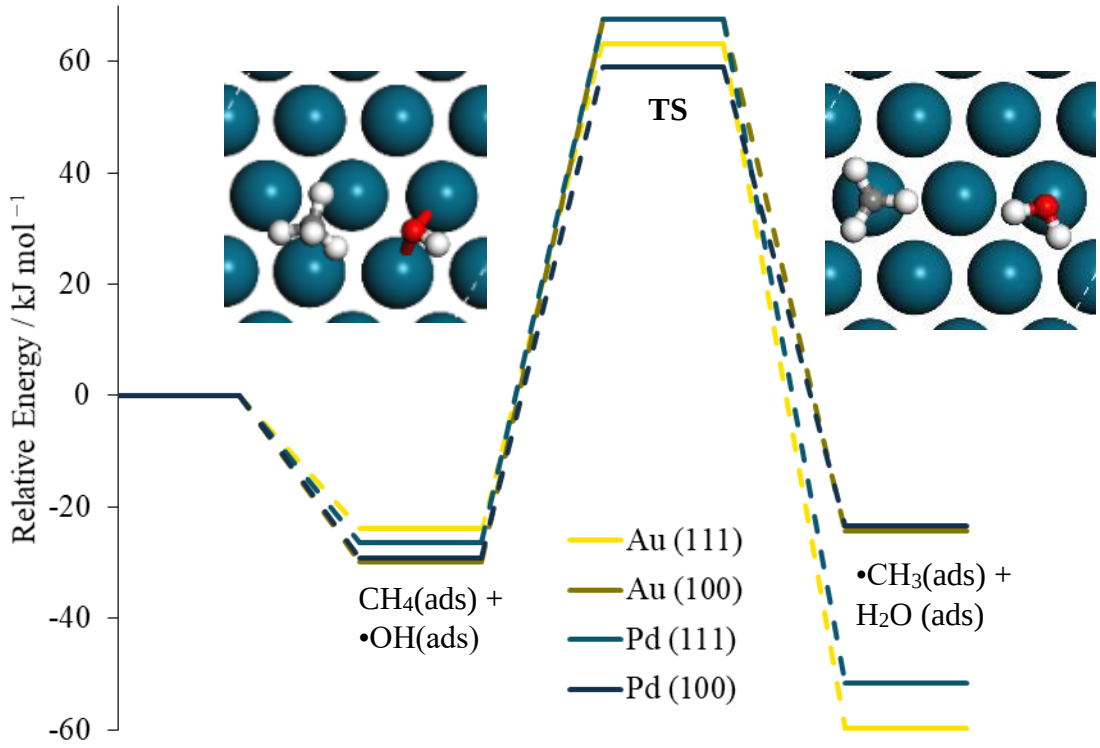


Figure 3: The calculated potential energy diagram for the abstraction of H from methane by surface OH, step **2**→**3**, Scheme 2 using Au(111) (yellow), Au(100) (orange), Pd(111) (blue) and Pd(100) (purple). Relative energy refers to the adsorption energy relative to the adsorbed OH and isolated methane. The inset graphics show structures for the example of Pd(111). M represents Au or Pd as appropriate. TS: transition state for the dissociation step. Atom colours on inset images: Au; yellow, Pd; blue, C; grey, O; red and H; white.

The products of this elementary step are a methyl radical and water. Both species are stabilised by adsorption at top sites in the optimised structures with the methyl group directly bonding to a metal atom (*e.g.* Figure 3, inset right). The overall energy profile shows that $\Delta E_R$ is negative (*i.e.* the step is exothermic) for the (111) surfaces and small but positive (Table 2, *i.e.* endothermic) on the (100) surfaces, indicating there is a stronger driving force for hydrogen abstraction on the (111) surfaces than over (100) surfaces. The reaction energy is also more negative for Au(111) than Pd(111) by some 11 kJ mol$^{-1}$. This reaction involves the breaking of a surface M-OH bond to be replaced by a much weaker adsorbed water interaction and the formation of a surface M-$CH_3$ bond from weakly physisorbed methane. The overall reaction energy will be determined by the balance of the surface M-OH/M-$CH_3$ interactions for each surface. Accordingly, the adsorption energies for the methyl radicals relative to gas phase •$CH_3$ and those for •OH(ads) relative to gas phase •OH were also calculated (Table 2). It is evident that the methyl radical is being stabilised by all four surfaces with the M-$CH_3$ distances close to the expected bond lengths from standard atomic radii (Au-C: 2.05 Å, Pd-C: 2.10 Å).[54] The shorter Pd-$CH_3$ distances are also consistent with the stronger methyl-surface bond on Pd than Au; for (111) surfaces $E_{ads}$($CH_3$) on Pd is more negative than on Au by 46 kJ mol$^{-1}$ while the corresponding difference for (100) surfaces is 35 kJ mol$^{-1}$. For both Pd and Au, shorter M-$CH_3$ bond lengths are found on the (100) surface than on the (111) and the methyl adsorption energy gives a stronger bond by 11 kJ mol$^{-1}$ for Au and 6 kJ mol$^{-1}$ for Pd. For the surface M-OH species, adsorption to Pd surfaces is around 60 kJ mol$^{-1}$ more favourable than to the corresponding Au surfaces and with each metal showing stronger binding of •OH(ads) on the (100) than on the close packed (111) surface. The differences in adsorption energy between (100) and (111) are more pronounced for •OH(ads) than seen for •$CH_3$(ads), with $E_{ads}$(OH) more favourable by 46 kJ mol$^{-1}$ on the Au(100) surface compared to the Au(111), the corresponding difference for Pd being 42 kJ mol$^{-1}$. Accordingly, the effect of the metal surface structure on the reaction energy for methane activation by •OH(ads), $\Delta E_R$ can be understood as an overall stronger binding of the formally radical species to the more open (100) surface than the (111) for which the difference is greater in the reactant state. We also note that the strongly negative values for $E_{ads}$(OH) and $E_{ads}$($CH_3$) in Table 2 indicate that the radicals are likely to be trapped on the surface rather than released into the reaction mixture.

Table 2 also lists the calculated barrier energies, $E_b$, for the H abstraction from methane by •OH(ads) over each of the surfaces. The barrier for the Au(111) surface, at 87 kJ mol$^{-1}$ is lower

than that for the Au(100) by 10 kJ $mol^{-1}$, whereas a barrier of 88 kJ $mol^{-1}$ is found on the Pd(100) surface and that on Pd(111) is higher by 6 kJ $mol^{-1}$. The structures of the transition states (figure S3) show that, for Pd surfaces, the hydroxyl radical remains in a bridge configuration, with the methyl radical being strongly stabilised by the surface, maintaining a Pd-$CH_3$ bond (≈ 2.2 Å) with only a minor increase in the Pd—OH distance compared to the optimised reactant state (Δ(Pd—OH) ≈ 0.1 Å (100) and Δ(Pd—OH) ≈ 0.2 Å (111)). In contrast, for the Au(111) surface, the hydroxyl radical moves away from the bridge configuration identified for adsorbed •OH(ads) on the surfaces to a top site in the transition state, so that a component of the barrier energy will be the breaking of an Au-OH bond. Even so, the hydrogen abstraction step has a lower energy barrier on the Au(111) surface than that on the Au(100). Yoshizawa and co-workers have reported a notably lower barrier ( 76 kJ $mol^{-1}$) for H abstraction from methane by surface OH species on Pd(111).[28] However, as those calculations use the PBE functional without dispersion correction they also note a weak interaction of methane with the surface ( $E_{ads}(CH_4)$ = -1 kJ $mol^{-1}$ ), our transition state energy relative to the Pd(111)OH surface and $CH_4$(g) is 68 kJ $mol^{-1}$, suggesting that the transition state is stabilised to a lesser extent by dispersion than is $CH_4$(ads).

Bader analysis for the transition state geometries is summarised in Table S5. In all cases there is electron donation from the surface to the •OH(ads) and the forming •$CH_3$(ads) radical is also found to carry a small negative charge. The •OH(ads) values are generally higher in each case than seen for the •OH(ads) species formed from $H_2O_2$ decomposition (Table S4). The transferring H atom carries a small positive charge of between 0.398 |*e*| and 0.434 |*e*|.

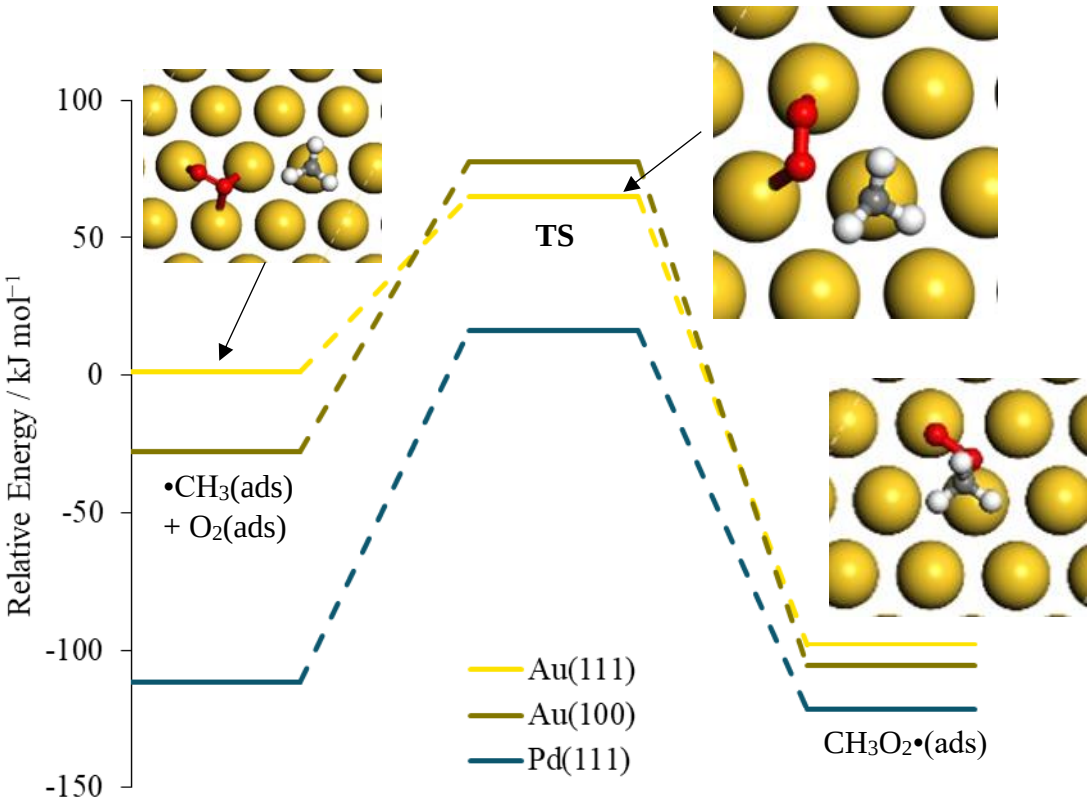


Figure 4: The calculated potential energy diagram for the reaction of •$CH_3$(ads) and $O_2$(ads) to form a surface bound methyl peroxy species $CH_3O_2$•(ads), step **4**→**5**, Scheme 2, using Au(111) (yellow), Au(100) (orange) and Pd(111) (blue). Relative energy is referred to the surface bound •OH(ads) species (**2**, Scheme 2) and the energies of other reagents, including eliminated water in isolation. The inset graphics show structures for the example of Au(111). TS: transition state for the $H_3C$-OO bond formation. Atom colours on inset images: Au; yellow, C; grey, O; red and H; white.

Overall the barriers found for the methane activation step over the two metals are remarkably similar which suggests that, once a surface •OH(ads) is formed, the activation of methane will proceed in a similar manner irrespective of the metal used.

*Formation of the Methyl Peroxy Intermediate*

After the molecular adsorption of dioxygen to the surface and displacement of water, to give $O_2$(ads) (step **3**→**4**, Scheme 2), the next step in the catalytic cycle stage of the proposed reaction mechanism is $H_3C$-$O_2$ bond formation between the surface methyl radical and co-adsorbed dioxygen. This leads to the formation of a methyl peroxy intermediate, $CH_3O_2$•(ads), (step **4**→**5**, Scheme 2). This is the precursor to methyl hydroperoxide, the primary intermediate observed experimentally.[24]

To study this step, co-adsorbed configurations of a methyl radical and molecular oxygen and adsorbed structures for the intermediate $CH_3O_2$•(ads) were optimised on the four metal surfaces. The calculated energies and geometric data is summarised for the methyl radical and $O_2$(ads) in Table 3 and that for the adsorbed methyl peroxy intermediate in Table 4. For the catalytic cycle we use the cycle start point of OH(ads) + $CH_4$(g) + $O_2$(g) as the reference to calculate the adsorption energies in Tables 3 and 4. The overall reaction profile for the two Au surfaces and for Pd(111) using the same reference is shown in Figure 4 and the case of Pd(100) is also discussed below.

Three different configurations were found for the methyl radical and molecular oxygen on the Au(100) (Figure S4). In each case, the methyl radical was in a top position with the M-$CH_3$ distances covering a very narrow range ( 2.037 – 2.099 Å ). In contrast, the co-adsorbed oxygen molecule could be optimised with the molecular axis parallel to the surface and both O atoms interacting with metal atoms, to give top-top (Figure S4*a*) or bridge-bridge (Figure S4*b*) configurations. In addition, the molecular axis of $O_2$(ads) could be set roughly perpendicular to the surface in an end-on bridge configuration (Figure S4*c*). The most stable structure on Au(100) has the oxygen molecule in the bridge-bridge configuration (Table 3) with each oxygen atom directly bonded to two gold atoms, the $E_{ads}$ value for this structure is 20 kJ $mol^{-1}$ and 47 kJ $mol^{-1}$ more negative than the top-top and end-on bridge alternatives, respectively. The end-on bridge structure has a positive calculated adsorption energy relative to the OH(ads) and isolated reactant molecules at the start of the catalytic cycle. The O-O bond distance calculated for $O_2$ in the triplet state in isolation is 1.234 Å and all of the structures reported in Table 3 show longer bond lengths than this reference, indicating that the molecule is activated by charge transfer from the surface. This was confirmed by Bader analysis (Table S6) which showed that the $O_2$(ads) structure with the molecular axis parallel to the surface has a charge of -0.590 |*e*| / -0.793 |*e*| for the top-top / bridge-bridge configurations, respectively. For end-on adsorption of $O_2$ the charge transfer from the surface is not as great ( molecular charge = -0.470 |*e*| ) with 60% of the charge assigned to the O atom closest to the surface. In contrast to $O_2$(ads), charge transfer to the •$CH_3$(ads) co-adsorbed species is less that 0.05 electrons in all cases. This may indicate that the more negative charge seen on $CH_3$ in the transition state for the $CH_3$-H bond activation by •OH(ads) is more to do with polarisation of the bond being cleaved than donation from the metal.

For the $CH_3O_2$•(ads) intermediate on the Au(100) surface, the end-on bridge configuration, is the lowest energy configuration (figure S5*a*, table 4), so that this intermediate is formed by the breaking of two Au—O bonds for one of the oxygen atoms in $O_2$(ads) as the bond with the methyl radical is formed. Even so, the adsorption energy is notably more negative than for •$CH_3$(ads) + $O_2$(ads), indicating that this step (**4**→**5**, Scheme 2) in the reaction is thermodynamically favourable. Bader analysis summarised in Table S7 shows that $CH_3O_2$•(ads) has also received some electron density from the surface with an overall charge for this species of -0.438 |*e*|, similar to that seen for •OH(ads).

The two most stable configurations of the adsorbed methyl radical and molecular oxygen from the Au(100) surface were constructed and optimised on the Pd(100) surface. The calculated adsorption energies are notably more negative for Pd(100) than for Au(100), (Table 3). For Pd(100) the structure with molecular oxygen adsorbed in a bridge-bridge configuration was also found to be more stable than that with the molecule in a top-top configuration, by 49 kJ mol$^{-1}$. The oxygen molecule adsorbed in a bridge-bridge position also has an O-O bond which is 0.092 Å longer than

Table 3: Energetic and geometric data for co-adsorbed •$CH_3$(ads) and $O_2$(ads).

| **Surface / $O_2$ position**[a] | $E_{ads}$[b] **/ kJ mol$^{-1}$** | **M-$CH_3$ / Å** | **M-O(O)**[c] **/ Å** | **O-O / Å** |
|---|---|---|---|---|
| Au(100)/t-t | -8 | 2.099 | 2.172-2.173 | 1.345 |
| Au(100)/b-b | -28 | 2.099 | 2.286-2.311 | 1.423 |
| Au(100)/b | +19 | 2.094 | 2.330-2.360 | 1.302 |
| Pd(100)/t-t | -99 | 2.040 | 2.002-2.013 | 1.341 |
| Pd(100)b-b | -148 | 2.037 | 2.100-2.107 | 1.433 |
| Au(111)/t-t | +22 | 2.040 | 2.277-2.293 | 1.323 |
| Au(111)/t-b | +1 | 2.037 | 2.417-2.611, 2.235 | 1.335 |
| Pd(111)/t-b | -112 | 2.056 | 2.135-2.141, 2.022 | 1.376 |

Note: *a*) Abbreviations t: top and b: bridge, *b*) Adsorption energy values are relative to the surface bound OH group (**2**, Scheme 2) and the energies of other reagents, including eliminated water in isolation, *c*) a dash is used to indicate the range of values, for t-b cases the single figure is for the t site.

seen for the top-top configuration and 0.199 Å than in $O_2$(g), indicating that the molecule is more strongly activated toward dissociation.

Bridge-bridge configurations for $O_2$(ads) co-adsorbed with •$CH_3$(ads) could not be obtained on the (111) surfaces. On the Au(111) surface both top-top and top-bridge configurations were stable, with the top-bridge giving the more favourable adsorption energy by 21 kJ mol$^{-1}$ (Table 3). Both

structures gave energies that are positive compared to the reference state of the start of the catalytic cycle, however, at only +1 kJ $mol^{-1}$, the top-bridge has practically the same calculated energy as this •OH(ads) + $CH_4$(g) + $O_2$(g) reference. Configurations that were constructed with molecular oxygen arranged top-top on the Pd(111) surface, switched to top-bridge on optimisation. Pd(111) also gave a much more favourable calculated adsorption energy of -112 kJ $mol^{-1}$, but with a less pronounced O-O bond elongation than seen for the Pd(100) bridge-bridge case.

On the Pd(111) surface, structures for the adsorbed methyl peroxy radical were obtained with top-top and top-bridge configurations (Figure S5*c* and S5*d*). The top-bridge structure has a slightly more favourable adsorption energy than the top-top ( by 4 kJ $mol^{-1}$, Table 4). In both structures, the $CH_3O$-O•(ads) bond was found to be elongated compared to the methyl peroxy radical in gas phase ($CH_3O$-O•(g) = 1.337 Å) and is closer to the value found for the free methyl hydroperoxide molecule ($CH_3O$-OH(g) = 1.474 Å). For the methyl peroxy radical in a top-top configuration, this elongation on the Pd (111) surface ($CH_3O$-O•(ads) = 1.463 Å) is similar to the more open Au(100) surface ($CH_3O$-O•(ads) = 1.467 Å). However, the $CH_3O$-O•(ads) bond distance for the optimised bridge-top configuration on Pd(111) has a much higher value of 1.667 Å, suggesting that the molecule is practically dissociated into a methoxy radical and an oxygen atom. Bader analysis (Table S7) shows that these $CH_3O_2$•(ads) species on Pd(111) also receive electron density from the surface with calculated charges of -0.564 |*e*| and -0.489 |*e*| for top-top and top-bridge adsorption, respectively.

The adsorption of the methyl peroxy radical on the Pd(100) surface resulted in cleavage of the $CH_3O$-O•(ads) bond without a barrier, forming a surface bound $CH_3O$•(ads) and an oxygen atom

Table 4: Energetic and geometric data for the adsorbed $CH_3O_2$•(ads) intermediate.

| **Surface / $CH_3O_2$• position**[a] | $E_{ads}$[b] **/ kJ $mol^{-1}$** | **M-$OOCH_3$**[c] **/ Å** | **M-$(O)OCH_3$**[c] **/ Å** | **$CH_3O$-O / Å** |
|---|---|---|---|---|
| Au(100)/b | -106 | 2.240-2.260 | ----- | 1.467 |
| Au(111)/t | -98 | 2.149 | ----- | 1.454 |
| Pd(111)/t-b | -122 | 2.054-2.060 | 2.198 | 1.667 |
| Pd(111)/t-t | -118 | 2.008 | 2.309 | 1.463 |

Note: *a*) Abbreviations t: top, h: hollow and b: bridge, *b*) Adsorption energy values are relative to the surface bound OH group (2, Scheme 2) and the energies of other reagents, including eliminated water in isolation, *c*) a dash is used to indicate the range of values, M-$(O)OCH_3$ refers to the metal to oxygen distance for the O atom bonded to the methyl group, "-----" is used to indicate that this O atom is not interacting with the surface.

occupying a hollow site. An adsorption energy -97 kJ $mol^{-1}$ was calculated for this dissociated state.

For the Au(111) surface, the lowest energy mode of adsorption of the $CH_3O_2$•(ads) intermediate was found to have an $\eta^1$ co-ordination the terminal O atom of the species in a top position and the O atom bonded to carbon away from the surface (Figure S5*b*). This structure has an adsorption energy lower in magnitude than found for other surfaces and the shortest $CH_3O$-O•(ads) (Table 4), and the calculated Bader charge is also the smallest in magnitude (-0.401 |*e*|, Table S7).

Using these optimised structures as end points for NEB calculations the barriers to the formation of the methyl peroxy radical on the Au surfaces from the •$CH_3$(ads) and $O_2$(ads) species were determined. The resulting transition state on the Au(100) surface (Figure S6*a*) shows that the bridge-bridge position of the oxygen molecule was maintained with a slight elongation of all four Au-O bonds. The bonds to the surface for the oxygen atom that is closest to the methyl group in the transition state are 2.286 Å and 2.430 Å in the co-adsorbed starting point but increase to 2.572 Å and 2.430 Å at the transition state. This leads to a lower calculated Bader charge for the $O_2$(ads) molecule at the transition state compared to the initial structure with $O_2$ and •$CH_3$ co-adsorbed, while the methyl radical has a small positive charge at this point in the reaction (Table S8).

Similarly, on the Au(111) surface the bridge-top position of the oxygen molecule was maintained for the $CH_3O_2$•(ads) forming transition state (Figure S6*b*). In this case the Au-O bond for the O atom in the bridge site is practically broken for the Au atom it has in common with the methyl group ( Au-O distance increases from 2.417 Å to 2.824 Å ) while the same oxygen has a shorter bond to its second Au neighbour at the transition state than was observed for the co-adsorbed starting point (2.589 Å *cf* 2.611 Å). In addition, the Au-O bond for the oxygen in the top position

increased from 2.235 Å for the •$CH_3$(ads) and $O_2$(ads) structure to 2.243 Å at the transition state on Au(111).

The top-bridge structure of the methyl peroxy radical on the Pd(111) surface shows it to be strongly activated, but not completely cleaved (Table 4, Figure S5*d*). Accordingly, an NEB calculation was also carried to identify the transition state for the formation of $CH_3O_2$•(ads) on this surface. The transition state structure obtained (Figure S6*c*) has a very similar geometry to that obtained on the

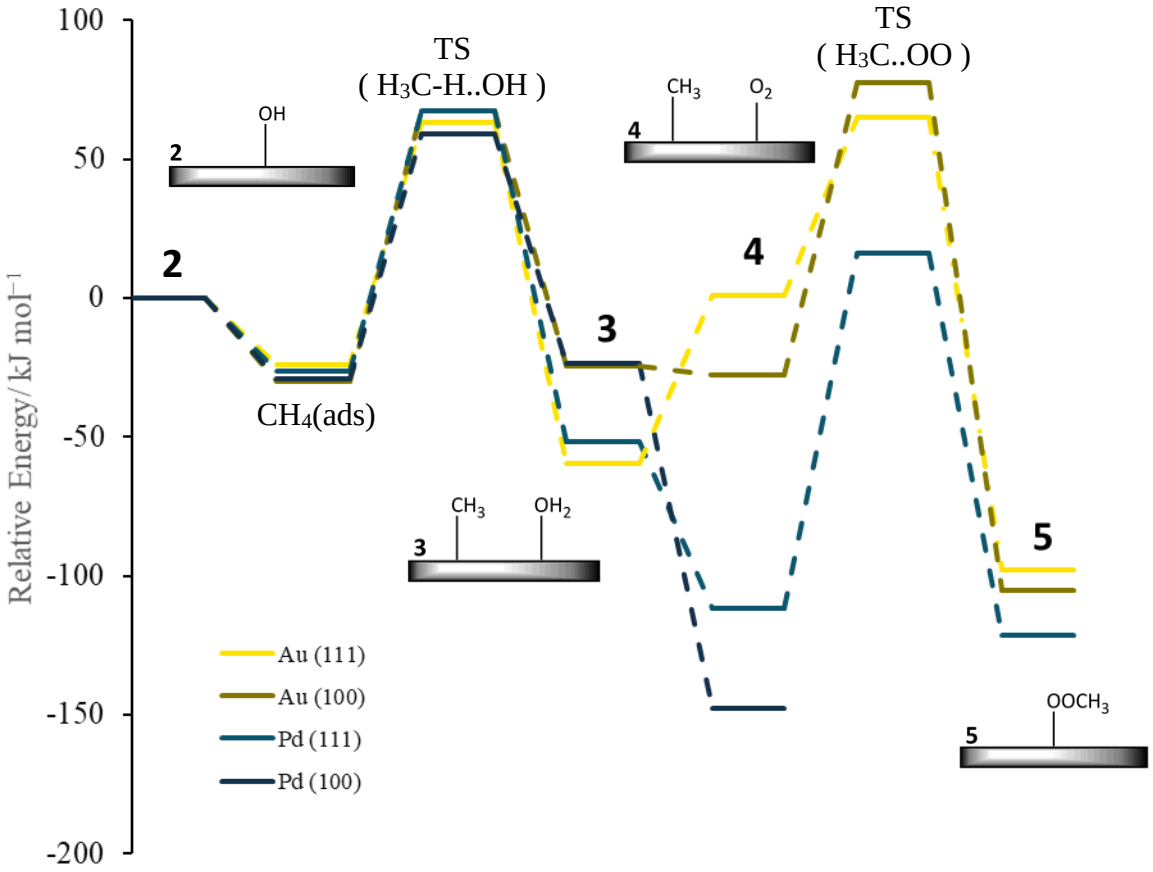


Figure 5: The calculated potential energy diagram for the complete catalytic cycle of Scheme 2 for Au(111) (yellow), Au(100) (orange), Pd(111) (blue) and Pd(100) (black). Relative energy refers to the surface bound •OH(ads) group (**2**, Scheme 2) and the energies of other reagents, including oxygen, methane and eliminated water in isolation as required. The inset graphics show the states from Scheme 2 and TS indicates transition state for process indicated.

Au(111) surface but with a shorter M-C ( 2.315 Å (Pd-C) *vs* 2.515 Å (Au-C)). These distances are very similar in the •$CH_3$(ads) and $O_2$(ads) co-adsorbed structure (Table 3), suggesting that the stabilisation of the methyl radical at the transition state on the Pd(111) surface is stronger than on

Au(111). Moreover, the oxygen molecule moves to a top-top configuration with Pd-O bond distances of 2.024 Å and 2.162 Å.

The barriers for the formation of the methyl peroxy radical relative to •$CH_3$(ads) and $O_2$(ads) on the Au(111), Au(100), and Pd(111) surfaces were found to be 64 kJ mol$^{-1}$, 105 kJ mol$^{-1}$ and 128 kJ mol$^{-1}$, respectively. Figure 4 shows that although the lowest barriers are seen for the Au surfaces this is largely due to the weak adsorption of the $O_2$ molecule relative to displaced water (which is included in the reference energies in this section) so that the lowest energy transition state on this scale is on the Pd(111) surface. As has been noted, the methy peroxy radical appears to be unstable on the Pd(100) and so would dissociate as the new C-O bond is being formed.

Table 5: Comparison of the adsorption energies for water and oxygen.

| **Surface** | $E_{ads}(\mathrm{H_2O{:}CH_3})^a$ **/ kJ mol$^{-1}$** | $E_{ads}(\mathrm{O_2{:}CH_3})^a$**/ kJ mol$^{-1}$** | $E_{ads}(\mathrm{O_2{:}CH_3}) - E_{ads}(\mathrm{H_2O{:}CH_3})$ **/ kJ mol$^{-1}$** |
|---|---|---|---|
| Au (111) | -35 | +26 | +61 |
| Pd (111) | -43 | -103 | -60 |
| Au (100) | -34 | -38 | -3 |
| Pd (100) | -49 | -174 | -124 |

Note: *a*) the $E_{ads}(\mathrm{X{:}CH_3})$ means that the adsorption energy of the species X has been calculated with •$CH_3$(ads) also present on the surface in both the adsorbed and surface reference states.

To gain a clearer comparison of methane oxidation to $CH_3O_2$•(ads) over the different surfaces Figure 5 brings together the calculated energies for the catalytic cycle of Scheme 2 on a consistent scale by plotting the total energy profile relative to the adsorbed hydroxyl radical at the start of the cycle with the reference energies of methane and oxygen included from calculations of these molecules in isolation.

On this scale, the energy barrier for methane activation is similar regardless of the metal or surface facet with the transition state ( TS ($H_3$C-H..OH) ) energies between 87 kJ mol$^{-1}$ and 97 kJ mol$^{-1}$ above the •OH(ads) and physisorbed $CH_4$ level (Table 2), the lowest barrier is actually seen for the Au(111) surface. There are more significant differences in the following step ( **3→4** ) in which the water produced on methane activation is displaced by oxygen adsorption to the surface. On the Au(111) surface the binding of water is actually stronger than that of molecular oxygen whereas for the Pd surface there is a significant lowering of the system energy when oxygen replaces water. In order to quantify this effect, Table 5 compares the adsorption energy of water ( $E_{ads}(\mathrm{H_2O{:}CH_3})$ ) and molecular oxygen ($E_{ads}(\mathrm{O_2{:}CH_3})$) in the presence of a methyl radical on each surface and

also gives the energy difference for the displacement of water by oxygen ($E_{ads}(O_2{:}CH_3)$-$E_{ads}(H_2O{:}CH_3)$).

The adsorption of water is favourable on all surfaces, having a narrow range of -34 kJ mol$^{-1}$ (Au(100)) to -49 kJ mol$^{-1}$ (Pd(100)), with the Pd surfaces showing a slightly higher affinity for water. The adsorption energy for molecular oxygen is notably more favourable on the Pd surfaces than on either Au facet, with the Pd(100) surface having a calculated $E_{ads}(O_2{:}CH_3)$ some 71 kJ mol$^{-1}$ more negative than Pd(111) and 136 kJ mol$^{-1}$ more negative than Au(100). The Au(111) surface has a positive calculated adsorption energy for $O_2$(ads) implying that its adsorption in the presence of a surface methyl radical is unfavourable even from the gas phase used in the reference calculation. The resulting $E_{ads}(O_2{:}CH_3) - E_{ads}(H_2O{:}CH_3)$ values presented in Table 5 imply that the displacement of water by oxygen is energetically unfavourable on Au(111) when •$CH_3$(ads) is also present, and the displacement of water by dioxygen has only a weak driving force on Au(100). In contrast, both Pd surfaces show very negative displacement energies, so that it would be expected that a Pd metal surface would readily adsorb molecular oxygen in the aqueous conditions used in methane oxidation reactions with colloidal nanoparticles at low temperature.[29] However, for Au(100) and the Pd(111) surfaces, the energy barriers for the next step of $H_3C\ldots O_2$ bond formation (**4**→**5**, Scheme 2), at 105 kJ mol$^{-1}$ (Au(100)) and 128 kJ mol$^{-1}$ (Pd(111)), are actually greater than that for the methane activation by •OH(ads), which makes it kinetically difficult to form the intermediate, $CH_3O_2$•(ads). As we have already noted, the $CH_3O_2$•(ads) is unstable on Pd(100) and decomposes to $CH_3O$•(ads) and O(ads).

Both Pd surfaces exhibited a high affinity for oxygen adsorption and so the cleavage of molecular oxygen was also studied using the example of Pd(111). The activation barrier for the dissociation of molecular oxygen was found to be 63 kJ mol$^{-1}$, which is around half the energy barrier needed for the formation of the methyl peroxy radical from a surface adsorbed methyl radical and molecular oxygen (128 kJ mol$^{-1}$). This result suggests that it is highly likely that molecular oxygen will cleave on the surface before it combines with the methyl radical needed to form the methyl peroxy intermediate. An even smaller barrier of 9 kJ mol$^{-1}$ was observed for the dissociation of oxygen on the Pd(100) surface suggesting that the Pd(100) surface will readily oxidise when molecular oxygen is introduced into the reaction mixture.

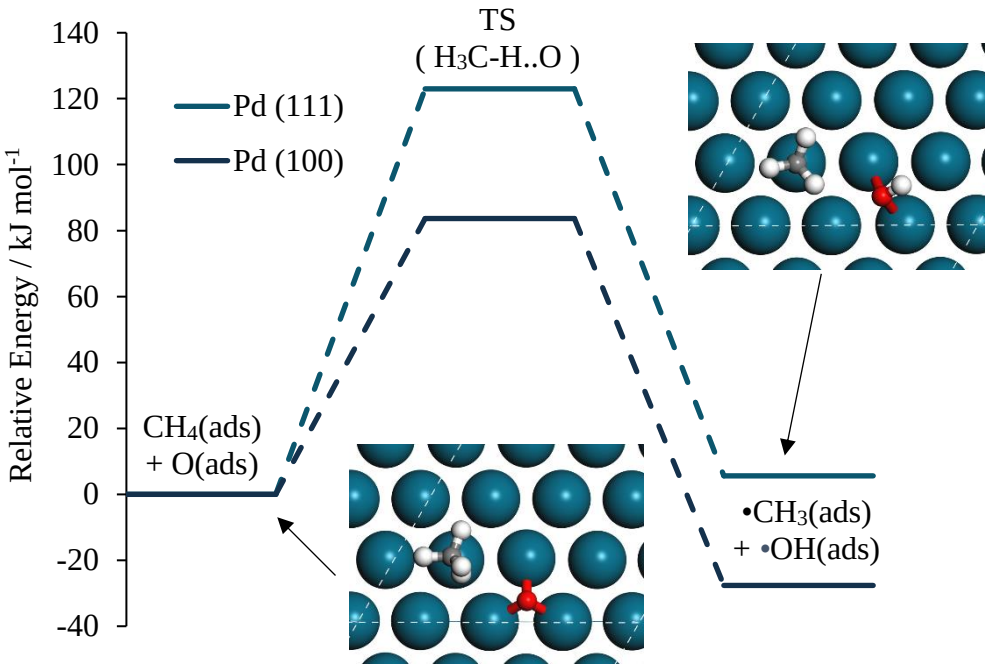


Figure 6: The calculated potential energy diagram for the activation of methane by O(ads) for Pd(111) (blue) and Pd(100) (black). Relative energy refers to the $CH_4$(ads) + O(ads) co-adsorbed state. The inset graphics show example structures from the Pd(111) case. Atom colours: Pd; blue, C; grey, O; red and H; white.

These observations mean that it is unlikely for a methyl peroxy radical to form on either the pure Au or pure Pd surfaces. The low affinity of the Au(111) surface for molecular oxygen will likely hinder the displacement of water by molecular oxygen resulting in blocking of the surface by water molecules in aqueous conditions. The affinity to molecular oxygen is higher on the Au(100) but the barrier for the formation of the methyl peroxy radical is also high (105 kJ $mol^{-1}$). The affinity of the Pd surfaces for oxygen results in low barriers for the cleavage of molecular oxygen and the formation of surface atomic oxygen species which will eventually form a PdO layer. Surface oxygen atoms are another possible species that could react directly with methane to activate the $H_3C$-H bond. Figure 6 shows the calculated potential energy profile for this process on Pd(100) and Pd(111). For each surface, the preferred mode of adsorption for the oxygen atom was a hollow position; 3-fold for Pd(111) and 4-fold for Pd(100). In both cases, methane adsorbs in a top position with only weak interaction with the surface. At the transition state for the hydrogen abstraction, the oxygen atom has moved to a bridge position which was maintained in the product state after the formation of the hydroxyl radical. This observation is consistent with our earlier finding that

•OH(abs) binds more strongly in a bridge configuration. In this case, the hydrogen of the hydroxyl radical is pointing away from the methyl radical which is located at a top site.

The barriers for the hydrogen abstraction from methane by an oxygen atom for the Pd(111), and Pd(100) were found to be 123 kJ $mol^{-1}$ and 84 kJ $mol^{-1}$ respectively. Comparison of these barriers with those calculated for H abstraction by •OH(abs) (Table 2) shows that the oxygen atom on Pd(111) would be expected to be much less reactive than the •OH(abs) species as the calculated barrier is some 26 kJ $mol^{-1}$ higher. In contrast, the oxygen atom on Pd(100) has a very similar barrier to that of •OH(abs) for hydrogen abstraction from methane ( 4 kJ $mol^{-1}$ lower ), and so would be expected to be competitive were both species present. We also considered the barriers for methanol formation on the Pd(111) and Pd(100) surfaces from the end point of the hydrogen abstraction process illustrated in Figure 6. Relative to the adsorbed methyl and hydroxyl radical the methanol formation barriers were found to be 149 kJ $mol^{-1}$ for Pd(111) and 155 kJ $mol^{-1}$ for Pd(100). These high activation energies suggest that it is unlikely that methanol can form on the pure Pd surfaces via the direct reaction of methyl radicals and •OH(abs), which gives a possible explanation for the experimental observation that the primary intermediate observed is methyl hydroperoxide and not methanol.[24] Moreover, the very low barrier for the oxygen cleavage on the Pd(100) surface means that the surface should be rapidly oxidised leaving few vacant metallic sites on which methyl radical can adsorb.

**iii) Formation and stability of methyl hydroperoxide**

At the end of the catalytic cycle shown in Scheme 2, we are left with a surface bound methyl peroxy species which must abstract a hydrogen atom from one of the chemical species in the reaction mixture in order to form the methyl hydroperoxide intermediate observed experimentally. The most likely source of hydrogen in the reaction mixture is $H_2O$, (**5**→**6**, Scheme 2) this process would also generate further hydroxyl radicals which can activate methane without the need for additional hydrogen peroxide. Abstraction of an H atom from water to complete the product formation is more likely than from hydrogen peroxide, not only because of their relative concentrations but also because work performed by Plauk *et al.*[55] has shown that the barrier for

the cleavage of the O-H bond in hydrogen peroxide is eight times higher than the barrier for the cleavage of HO-OH on the Pd(100) surface and more than three times higher on the Pd(111).

Once formed, methyl hydroperoxide has to adsorb and cleave in order to produce methanol (**6**→**7** and **7**→**8**, Scheme 2). In order to understand how the different surfaces activate methyl hydroperoxide for this process, different adsorption configurations of the primary intermediate were optimised on the four surfaces and the energy barrier for the cleavage of the $CH_3O$-OH(ads) bond was studied. The resulting adsorption energies and geometries are summarised in Table 6 and geometries are shown in figure S7.

Table 6: The calculated adsorption energies and geometry for methyl hydroperoxide.

| **Surface / $CH_3O_2H$ position**[a] | $E_{ads}$[b] **/ kJ mol$^{-1}$** | **M-O[c]/ Å** |
|---|---|---|
| Au(111)/b-t | -53 | 2.771 |
| Au(111)/h-t | -53 | 2.864 |
| Au(100)/h-t | -56 | 2.747 |
| Pd(111)/b-t | -69 | 2.308 |
| Pd(111)/t-t | -66 | 2.574 |
| Pd(111)/h-t | -70 | 2.409 |
| Pd(100)/h-t | -69 | 2.344 |
| Pd(100)/t-t | -70 | 2.360-2.399 |

Notes: *a*) Abbreviations t: top, h: hollow and b: bridge, *b*) Adsorption energy values are relative to the clean surface and isolated $CH_3O_2H$. *c*) M-O distances refer to the O atom closest to the surface.

Initially we examined top-top configurations on each surface since this has been suggested as a likely mode of adsorption of the methyl hydrogen peroxide on an alloy surface.[56] However, as the O—O bond distance is much smaller than the Pd—Pd (~2.7 Å) or the Au—Au (~2.9 Å) distances, the geometry of such structures is generally not stable and one of the oxygen atoms moves closer to the surface than the other. Even so, for all the configurations obtained, at least one of the oxygen atoms is in a top position while the second may move to a hollow or bridge location. In addition the OH group of the molecule may be orientated with the H down toward the surface ( *e.g.* Pd(111)/h-t shown inset in Figure 7 ), as was seen for the case of hydrogen peroxide earlier. The adsorption energies given in Table 6, show that the Miller index of the surface and the location of the adsorbate has quite a small influence on the adsorption energy, while the adsorption of $CH_3O_2H$ to Pd surfaces is generally around 15 kJ mol$^{-1}$ more energetically favourable than adsorption of the molecule on Au.

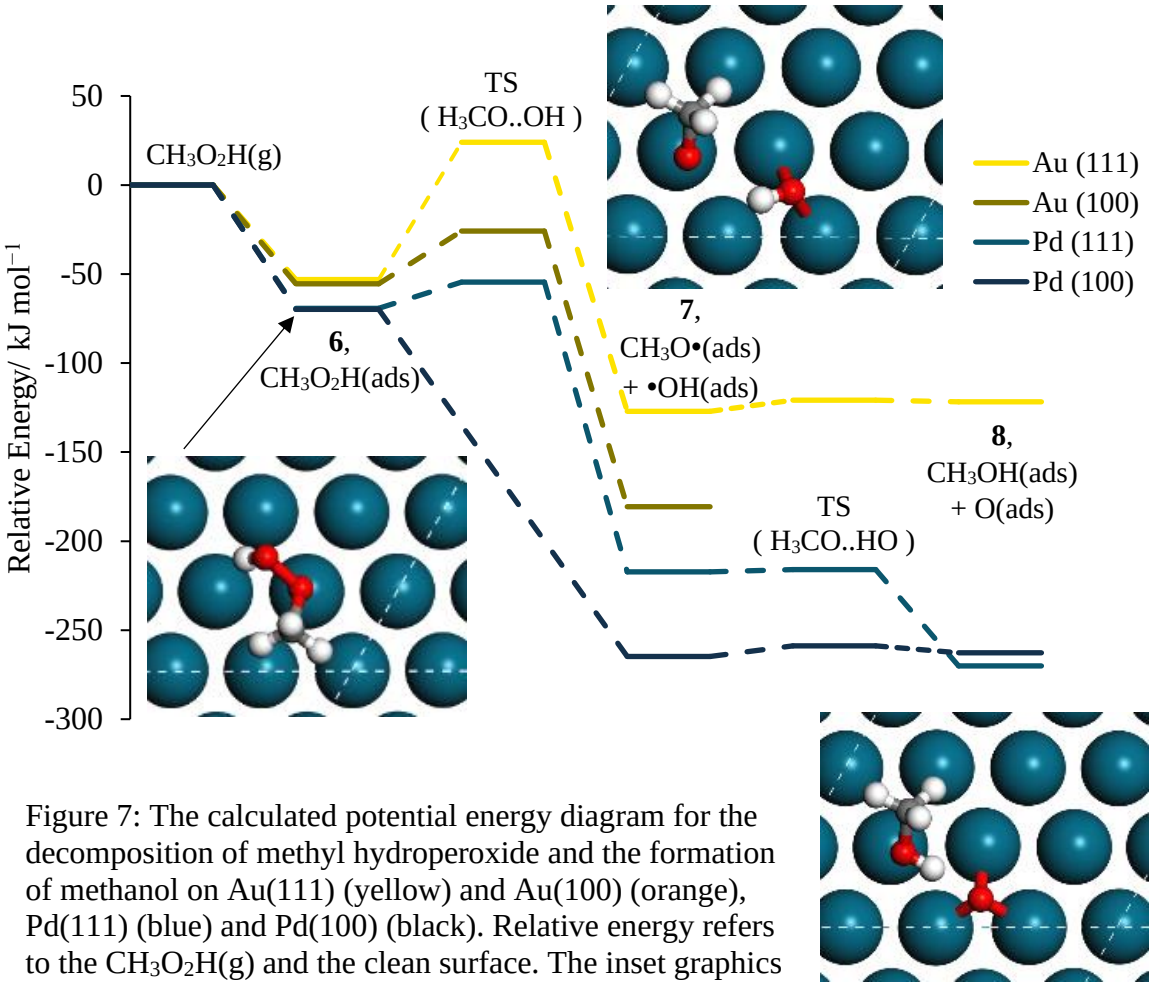


Figure 7: The calculated potential energy diagram for the decomposition of methyl hydroperoxide and the formation of methanol on Au(111) (yellow) and Au(100) (orange), Pd(111) (blue) and Pd(100) (black). Relative energy refers to the $CH_3O_2H$(g) and the clean surface. The inset graphics show example structures from the Pd(111) case. Atom colours: Pd; blue, C; grey, O; red and H; white.

Figure 7 shows the potential energy surface calculated for the cleavage of the $H_3CO$-OH(ads) bond over the four surfaces studied. Methyl hydroperoxide cleaves without an activation barrier on the Pd(100) surface *i.e.* dissociative adsorption, which is probably due to the top-top configuration for $CH_3O_2H$(ads) obtained for the Pd(100) surface (Table 6) whereby the interaction of both oxygen atoms with surface Pd atoms facilitates cleavage of the intermediate. The barriers for the cleavage of $H_3CO$-OH(ads) on the Pd (111), Au(100) and Au(111) were found to be 15 kJ $mol^{-1}$, 30 kJ $mol^{-1}$ and 77 kJ $mol^{-1}$, respectively. Lower barriers were also seen for Pd surfaces than for Au surfaces for the HO-OH(ads) bond breaking barrier in Table 1, although the Pd(111) surface was found to give the lowest barrier in that case.

To produce methanol, there has to be a hydrogen transfer to the methoxy radical formed on breaking the $H_3CO$-OH bond. This could come from the hydroxyl radical which is the other product of this step or from co-adsorbed water. The barrier for the hydrogen transfer step from the •OH(abs) was found to be very small for three of the surfaces (Au(111): 6 kJ $mol^{-1}$, Pd(111): 1 kJ $mol^{-1}$, Pd(100): 6 kJ $mol^{-1}$). These small barriers for the hydrogen transfer along with the relatively low energy barriers for the cleavage step show that once the methyl hydroperoxide intermediate is formed, the process of methanol formation is straightforward on Pd surfaces. The case of Au is not so clear cut, the optimisation of structure **8** (Figure 7, $CH_3OH$(ads) and O(ads)) on the Au(111) surface places this end point only just below the transition state of the H transfer step, and so the reverse barrier to reform the •$OCH_3$(abs) + •OH(abs) intermediates is preferred. Indeed, for the Au(100) surface, optimisation of structure **8** resulted in the back transfer of the hydrogen to the surface oxygen atom and so the methanol formation step is not shown for that surface in Figure 7.

To summarise this section on the catalytic cycle and production of methanol. Pd surfaces show a higher affinity for the cleavage of hydrogen peroxide than do Au surfaces. The hydrogen abstraction step from methane is about the same for both metals with barriers ranging from 87-97 kJ $mol^{-1}$. The formation of the methyl peroxy radical through the incorporation of $O_2$(ads) into the scheme shows more variation between metals and surfaces. The high affinity of Pd surfaces for molecular oxygen is likely to result in the formation of a PdO surface, whilst the low affinity of the Au surfaces for molecular oxygen will lead to inhibition of catalytic activity due to competition with molecularly adsorbed water.

**Effects of alloying metals on key steps**

We have used the data presented so far to argue that there are different factors for the Au and Pd surfaces which affect the ability of these metals to act as catalysts. Over Pd surfaces, the barriers to the cleavage of dioxygen are very low, leading to ready oxidation of the surfaces to form an oxide overlayer. Although Au is less readily oxidised, the competitive adsorption of water for reactions in aqueous media will tend to limit the adsorption of dioxygen and so the reaction rate will be low (Figure 5, Table 5). Experimentally, catalysts formed from mixed AuPd colloids show significantly higher rates of reaction for the methane to methanol reaction[24] and so in this section, we consider the effect of adding single Au atoms to our Pd surfaces and of adding single Pd atoms to our Au surfaces. We have also focused on the key steps identified that limit activity for the pure

metals; the formation of a surface oxide for Pd and the competition between oxygen and water over Au. To indicate the level of substitution made we will refer to the composition of the surface layer, for example, $Au_1Pd_{15}(111)$ refers to a simulation slab used for the Pd(111) surface in which a single Pd atom has been replaced by Au. All slabs are still 5 layers so that in this example the slab would have four layers of Pd below the surface with an overall composition of $Au_1Pd_{79}$. The unit cell used for the surface simulation with metal substitution in this way remains fixed at the dimensions employed for the pure surface.

Table 7: Comparison of oxygen adsorption and dissociation over pure Pd and Pd with single Au atom substitution in surface layer.

| **Surface / $O_2$(ads) position**[a] | $E_{ads}(Pd_N)^{b,c}$ / kJ mol$^{-1}$ | $E_{ads}(Au_1Pd_{N-1})^{b,c}$ / kJ mol$^{-1}$ | $E_b$(O-O) / kJ mol$^{-1}$ | |
|---|---|---|---|---|
| | | | $Pd_N$[c] | $Au_1Pd_{N-1}$[c] |
| Pd(100)/b-b | −177 | −128 | 9 | 18 |
| Pd(111)/t-b | −100 | −40 | 63 | 74 |
| Pd(111)/t-t | ---- | −89 | ---- | 122 |

Notes: *a*) Abbreviations t: top, and b: bridge, *b*) Adsorption energy values are relative to the clean surface and isolated $O_2$, *c*) *N* gives the number of Pd atoms in the surface layer, Pd(111); *N*=16, Pd(100); *N*=18, in all cases the simulation slab consists of five layers with only the first layer having a Pd atom replaced by Au.

Table 7 compares the calculated adsorption energies for molecular oxygen and barriers to dissociation of $O_2$(ads) on Pd surfaces and the effect of adding a single Au atom to Pd(111) and to Pd(100) and Figure 8 shows the calculated structures for $O_2$(ads) for the $Au_1Pd_{N-1}$ cases. The bridge-bridge configuration of molecular oxygen observed on the pure Pd(100) is maintained when one of the co-ordinating Pd atoms is replaced by (Figure 8*a*). However, the oxygen atom bond to Pd is notably shorter than that to the Au substituent ( Pd-O; 2.087 Å *vs* Au-O; 2.407 Å), this Pd-O distance is also slightly shorter than seen on the pure Pd(100) surface (Table 2). On the $Au_1Pd_{15}(111)$ surface, two top-bridge configurations were examined; in the first the oxygen in the top position is binding to the substituent Au atom (Figure 8*b*) and in the second the oxygen in the bridge position is binding to the Au atom and a Pd surface atom. On optimisation, the second case switched to a top-top configuration with both oxygen atoms binding to Pd atoms (Figure 8*c*). The top-top configuration on $Au_1Pd_{15}(111)$ was found to be more stable than the top-bridge configuration by 49 kJ mol$^{-1}$, even though the bond lengthening and charge transfer effects associated with adsorption occur to a lesser extent for the top-top structure (Table S8). Table 7

also shows that the most stable oxygen adsorption geometry on $Au_1Pd_{15}(111)$ is still some 11 kJ $mol^{-1}$ less stable than the top-bridge arrangement on the pure Pd(111) surface.

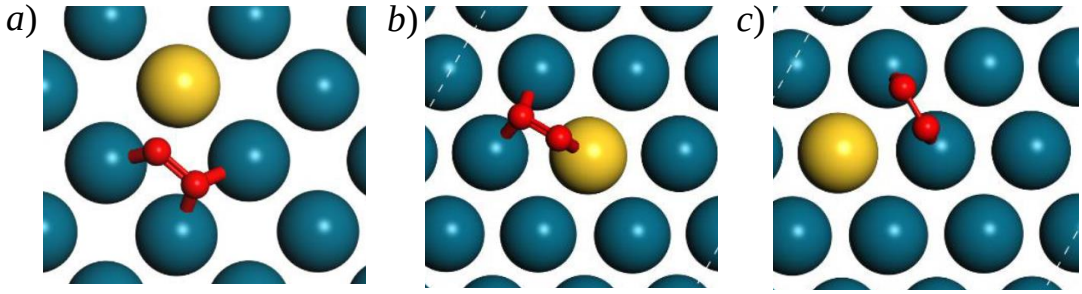


Figure 8: Optimised structures of $O_2$(ads) on *a*) $Au_1Pd_{17}(100)$/bridge-bridge, *b*) $Au_1Pd_{15}(111)$/top-bridge and *c*) $Au_1Pd_{15}(111)$/top-top. Atom colours: Au; yellow, Pd; blue and O; red.

The data in Table 7 also shows that the barriers to dissociation on the $Au_1Pd_{N-1}$ surfaces are higher than those found for the pure Pd surface, by 9 kJ $mol^{-1}$ for Pd(100) and 11 kJ $mol^{-1}$ for Pd(111) with oxygen in the top-bridge configuration. The more stable top-top configuration found for $Au_1Pd_{15}(111)$ has the highest barrier to oxygen dissociation at 122 kJ $mol^{-1}$. These results suggest that even the introduction of a single Au atom to a Pd surface can decrease the affinity of the Pd surfaces to molecular oxygen, thus decreasing the likelihood of the formation of an oxide surface.

The effect of the added Au atom on the formation of $CH_3O_2$•(ads) was considered by further calculations on the reaction of $CH_3$•(ads) and $O_2$(ads) on the $Au_1Pd_{15}(111)$ surface, *i.e.* **4**→**5** in Scheme 2. To ensure barriers for the doped and pure surface could be directly compared, the starting point of the NEB was the same for both transition state calculations whereby the oxygen was in a top-bridge position interacting with three Pd atoms and the methyl was on top of a Pd atom. For the doped surface, two of the Pd atoms involved are also neighbours of the surface Au atom (Figure S8).

The geometry of the calculated transition state for $Au_1Pd_{15}(111)$ closely resembled that for the pure Pd(111) surface, with the oxygen molecule switching into a top-top position and the carbon of the methyl radical pointing towards the oxygen as shown in Figure S6*c*. Even so, the calculated energy barrier for the formation of the $CH_3O_2$•(ads) on the $Au_1Pd_{15}(111)$ surface was 8 kJ $mol^{-1}$ lower than that for the $Pd_{16}(111)$ case ($Au_1Pd_{15}(111)$: 120 kJ $mol^{-1}$ *cf* $Pd_{16}(111)$: 128 kJ $mol^{-1}$). These calculations suggest that the introduction of Au into largely Pd rich surfaces leads to a lower affinity for $O_2$(ads), increasing the barrier to the oxygen cleavage required for PdO formation and

lowers the barrier to the formation of the methyl hydroperoxide primary intermediate in the methane to methanol reaction.

At the other end of the AuPd alloy composition range, we have considered the effect of a single Pd atom introduced into the Au(111) and Au(100) surfaces. These slabs with $Au_{15}Pd_1$(111) and $Au_{17}Pd_1$(100) top most layers were used to calculate the energy for the displacement of water by molecular oxygen in the presence of a methyl radical. Again, similar structures for the co-adsorbed $O_2$(ads) and •$CH_3$(ads) to those found for the pure $Au_{16}$(111) and $Au_{18}$(100) surfaces were created to allow direct comparison with the earlier results. The methyl radical was on a top site with the $O_2/H_2O$ directly interacting with the dopant Pd atom. For $Au_{15}Pd_1$(111) molecular oxygen was initially placed in a top-bridge adsorption mode with the oxygen atom in the bridge position interacting with both Au and Pd. On optimisation, the oxygen atom in the bridge site moved into a Pd top position, 2.809 Å away from the nearest Au atom. In the case of $Au_{17}Pd_1$(100), molecular oxygen was adsorbed in a bridge-bridge position mimicking that found with the $Au_{18}$(100) slab model. Two different configurations for $O_2$(ads) were examined for $Au_{17}Pd_1$(100) the first with the added Pd atom neighbouring the Au top site containing •$CH_3$(ads) (Figure S9*a*) and the second with the O atom nearest to the •$CH_3$(ads) in the bridge site between two Au atoms (Figure S9*b*). The configuration in which the Pd atom is a first neighbour to the Au atom at which the methyl radical is adsorbed was found to have a calculated adsorption energy only 3 kJ $mol^{-1}$ more favourable than the alternative setting.

Table 8 gives the calculated adsorption energies for water and dioxygen on the Au surfaces with a single Pd atom added and with co-adsorbed •$CH_3$(ads) along with the calculated displacement for water by oxygen, step **3**→**4**, that was highlighted in the discussion of Figure 5 as a difficult step for the pure Au surfaces. The effect of substituting one Au atom with Pd in the Au(111) surface is significant, both water and oxygen interact more strongly with the Pd doped surface. Molecular oxygen has an energetically unfavourable adsorption energy on Au(111) (Table 5) but on $Au_{15}Pd_1$(111) this changes to an energetically favourable situation with a calculated $E_{ads}$ of -43 kJ $mol^{-1}$. Water is also more strongly bound to $Au_{15}Pd_1$(111) but only by 11 kJ $mol^{-1}$ compared to the Au(111) case. This results in a reduction of the energy of the displacement reaction from +61 kJ $mol^{-1}$ for Au(111) to just to +2 kJ $mol^{-1}$ on $Au_{15}Pd_1$(111). For Au(100) the substitution of an Au atom by Pd is less dramatic but the displacement of water by $O_2$ is still enhanced. For

Au(100), $E_{ads}(O_2{:}CH_3) - E_{ads}(H_2O{:}CH_3)$ gives a value of -3 kJ mol$^{-1}$ (Table 5) indicating that this process would be practically thermodynamically neutral, whereas for $Au_{17}Pd_1(100)$ the displacement becomes more favourable with an energy difference for $H_2O$(ads) displacement by $O_2$ of -11 kJ mol$^{-1}$ (Table 8).

The energy barrier for the formation of the methyl peroxy radical on $Au_{15}Pd_1(111)$ was also calculated. Two different transition states were considered. In the first the new $H_3C..O_2$ bond is formed with the O atom at the Pd top site and in the second the oxygen atom was co-ordinated to an Au atom in the start point for the NEB calculation. The barrier for the case with bond formation taking place over Au was found to be 88 kJ mol$^{-1}$, some 28 kJ mol$^{-1}$ lower in energy than the transition state in which the oxygen atom is initially co-ordinated to Pd. This can be rationalised from the relative metal oxygen bond strengths and the fact that the reaction of $O_2$(ads) via the O atom at Pd will result in a $CH_3O_2$•(ads) intermediate at an Au top site.

Both barriers are higher in energy than those for the pure Au(111) surface (64 kJ mol$^{-1}$), which may be expected as the binding of molecular oxygen to Pd is stronger than to Au. Even so, the $Au_{15}Pd_1(111)$ surface still has a lower barrier for the formation of $CH_3O_2$•(ads) than is required for methane activation on the metal surfaces studied earlier and so the increased availability of $O_2$(ads) we have observed over the Pd substituted Au(111) surface would be expected to enhance the reactivity of Au catalysts overall.

Table 8: Comparison of the adsorption energies for water and oxygen on $Au_{N-1}Pd_1$ surfaces.

| **Surface** | $E_{ads}(H_2O{:}CH_3)^c$ **/ kJ mol$^{-1}$** | $E_{ads}(O_2{:}CH_3)^c$ **/ kJ mol$^{-1}$** | $E_{ads}(O_2{:}CH_3) - E_{ads}(H_2O{:}CH_3)$ **/ kJ mol$^{-1}$** |
|---|---|---|---|
| $Au_{15}Pd_1(111)$ | -46 | -43 | +2 |
| $Au_{17}Pd_1(100)^a$ | -47 | -58 | -11 |
| $Au_{17}Pd_1(100)^b$ | -47 | -55 | -8 |

Notes: Note: *a*) configuration as shown in Figure S9*a*, *b*) configuration as shown in figure S9*b*, *c*) the $E_{ads}(X{:}CH_3)$ means that the adsorption energy of the species X has been calculated with •$CH_3$(ads) also present on the surface in both the adsorbed and surface reference states.

The formation of the methyl peroxy radical on the $Au_{17}Pd_1(100)$ surface was also considered for two configurations of the start point and transition state differing in the positions of the reacting species relative to the Pd substituent. Starting with the $O_2$(ads) molecule in the favoured bridge-bridge arrangement and •$CH_3$(ads) at an Au top site the transition state can either have the $H_3C..O_2$ bond forming over a Pd atom (Figure S9*a* and *c*) or over an Au atom (Figure S9*b* and *d*).

Interestingly, the energy barrier for the formation of the methyl peroxy radical over the Au atom (106 kJ $mol^{-1}$) was found to be similar to the value obtained on the pure Au(100) surface (105 kJ $mol^{-1}$, Figure 4). A lower energy barrier of 92 kJ $mol^{-1}$ was found when the $H_3C..O_2$ bond is formed over a Pd atom (Figure S9*a* and *c*). In this transition state, the methyl radical is bonded to Pd with a calculated Pd-$CH_3$ bond length of 2.260 Å whereas for the transition state formed over Au (Figure S9*b* and *d*), the methyl radical has an Au-$CH_3$ bond distance of 2.460 Å. For Pd this interaction is 0.227 Å longer than seen for •$CH_3$(ads) on Pd(100) (Table 2) but for the transition state over Au on the $Au_{17}Pd_1$(100) surface, the Au-$CH_3$ is some 0.358 Å longer than seen on Au(100) (Table 2). In addition, Table 2 also shows that the •$CH_3$(ads) adsorption energy is 35 kJ $mol^{-1}$ more negative on Pd(100) than for Au(100). So it appears that the transition state formed over Pd in $Au_{17}Pd_1$(100) has a lower energy because the Pd substituent stabilises the methyl radical during the bond forming process.

**Summary and Conclusions**

We have provided a detailed analysis of each elementary step in the pathway for the incorporation of $O_2$(g) into the partial oxidation of $CH_4$ using Au and Pd catalysts with $H_2O_2$ as an initiator. Hydrogen peroxide readily dissociates on both Au and Pd surfaces to produce surface bound radical species, •OH(ads), with a very low barrier on Pd ( Pd(111): 5 kJ $mol^{-1}$ and Pd(100): 22 kJ $mol^{-1}$) and with a relatively low barrier over Au ( Au(111): 57 kJ $mol^{-1}$ and Au(100): 38 kJ $mol^{-1}$ ). So that, under experimental conditions[24] ( T = 50 °C ), we would expect these species to be present on the surfaces of catalysts formed from Au or Pd.

Over all the pure metal surfaces studied here, the initial activation of methane by reaction with •OH(ads) to produce •$CH_3$(ads) and water, proceeds with similar calculated barriers (between 87 kJ $mol^{-1}$ and 97 kJ $mol^{-1}$, Table 2). The methyl radical produced also binds strongly to either Pd or Au surfaces. For Pd(111) there is then a reaction pathway to $CH_3O_2$•(ads) but for Pd(100) the $CH_3O$-O(ads) bond is cleaved as we attempt to form this intermediate species, highlighting the much stronger affinity of Pd for oxygen compared to Au. Indeed, on both Pd surfaces studied, molecular oxygen is readily dissociated suggesting that a surface PdO layer would be formed under reaction conditions, preventing the formation of the methyl hydroperoxide intermediate which is observed experimentally.[29]

In contrast $O_2$(ads) does not dissociate on the Au(111) or Au(100) surface. However, the calculated energies for competitive adsorption with water from the aqueous solvent (Table 5) points to very low surface oxygen availability and the calculated barriers for $H_3C..O_2$ bond formation are actually higher than the initial barriers for the activation of methane by •OH(ads).

Modelling of the pure metal surfaces has identified limitations in their ability to catalyse the oxidation of methane to methanol for the reasons discussed above. Experimentally the use of AuPd alloy nanoparticles is found to give much better performance than seen for either pure metal.[24] In the final section of this work we covered calculations on the key reaction steps with surfaces of Pd with a single Au substitutent and surfaces of Au with a single Pd atom replacing a single Au atom. For the Pd case the Au substituted surface showed a lower affinity to $O_2$ and so would be expected to inhibit oxide formation. While for the Au surface with a Pd substituent the relative adsorption energies for water and $O_2$ favour oxygen in the vicinity of the Pd atom. Both effects would be expected to improve catalytic performance and so give some insight into the role of alloys in this catalysis.

Overall, these results demonstrate the role played by each metal in the colloidal alloy nanoparticles and show that there is also the possibility of further refining the catalyst composition and surface structure to improve activity further.

**Acknowledgements**

AN would like to thank Cardiff University for PhD funding. Computing facilities for this work were provided by Supercomputing Wales (Raven, HPC-Wales, and Hawk) and via our membership of the UK's HEC Materials Chemistry Consortium, which is funded by EPSRC (EP/L000202), this work used the UK Materials and Molecular Modelling Hub for computational resources, MMM Hub, which is partially funded by EPSRC (EP/P020194). JE would like to thank the Deutsche Forschungsgemeinschaft (DFG) for support through a research fellowship (EN 1229/1-1).

**References:**

(1) Alvarez-Galvan, M. C.; Mota, N.; Ojeda, M.; Rojas, S.; Navarro, R. M.; Fierro, J. L. G. Direct Methane Conversion Routes to Chemicals and Fuels. *Catal. Today* **2011**, *171* (1), 15–23. https://doi.org/10.1016/J.CATTOD.2011.02.028.

(2) Guo, X.; Fang, G.; Li, G.; Ma, H.; Fan, H.; Yu, L.; Ma, C.; Wu, X.; Deng, D.; Wei, M.; Tan, D.; Si, R.; Zhang, S.; Li, J.; Sun, L.; Tang, Z.; Pan, X.; Bao, X. Direct, Nonoxidative Conversion of Methane to Ethylene, Aromatics, and Hydrogen. *Science* **2014**, *344* (6184), 616–619. https://doi.org/10.1126/science.1253150.

(3) Rostrup-Nielsen, J. R.; Sehested, J. Hydrogen and Synthesis Gas by Steam- and CO2 Reforming. *Adv. Catal.* **2002**, *47*, 65–139. https://doi.org/10.1016/S0360-0564(02)47006-X.

(4) Götz, M.; Lefebvre, J.; Mörs, F.; McDaniel Koch, A.; Graf, F.; Bajohr, S.; Reimert, R.; Kolb, T. Renewable Power-to-Gas: A Technological and Economic Review. *Renew. Energy* **2016**, *85*, 1371–1390. https://doi.org/10.1016/j.renene.2015.07.066.

(5) Kirschke, S.; Bousquet, P.; Ciais, P.; Saunois, M.; Canadell, J. G.; Dlugokencky, E. J.; Bergamaschi, P.; Bergmann, D.; Blake, D. R.; Bruhwiler, L.; Cameron-Smith, P.; Castaldi, S.; Chevallier, F.; Feng, L.; Fraser, A.; Heimann, M.; Hodson, E. L.; Houweling, S.; Josse, B.; Fraser, P. J.; Krummel, P. B.; Lamarque, J.-F.; Langenfelds, R. L.; Le Quéré, C.; Naik, V.; O'Doherty, S.; Palmer, P. I.; Pison, I.; Plummer, D.; Poulter, B.; Prinn, R. G.; Rigby, M.; Ringeval, B.; Santini, M.; Schmidt, M.; Shindell, D. T.; Simpson, I. J.; Spahni, R.; Steele, L. P.; Strode, S. A.; Sudo, K.; Szopa, S.; van der Werf, G. R.; Voulgarakis, A.; van Weele, M.; Weiss, R. F.; Williams, J. E.; Zeng, G. Three Decades of Global Methane Sources and Sinks. *Nat. Geosci.* **2013**, *6* (10), 813–823. https://doi.org/10.1038/ngeo1955.

(6) Aricò, A. S.; Srinivasan, S.; Antonucci, V. DMFCs: From Fundamental Aspects to Technology Development. *Fuel Cells* **2001**, *1* (2), 133–161. https://doi.org/10.1002/1615-6854(200107)1:2<133::AID-FUCE133>3.0.CO;2-5.

(7) Xu, M.; Lunsford, J. H.; Goodman, D. W.; Bhattacharyya, A. Synthesis of Dimethyl Ether (DME) from Methanol over Solid-Acid Catalysts. *Appl. Catal. Gen.* **1997**, *149* (2), 289–301. https://doi.org/10.1016/S0926-860X(96)00275-X.

(8) Fazlollahnejad, M.; Taghizadeh, M.; Eliassi, A.; Bakeri, G. Experimental Study and Modeling of an Adiabatic Fixed-Bed Reactor for Methanol Dehydration to Dimethyl Ether. *Chin. J. Chem. Eng.* **2009**, *17* (4), 630–634. https://doi.org/10.1016/S1004-9541(08)60255-4.

(9) Waters, T.; O'Hair, R. A. J.; Wedd, A. G. Catalytic Gas Phase Oxidation of Methanol to Formaldehyde. *J. Am. Chem. Soc.* **2003**, *125* (11), 3384–3396. https://doi.org/10.1021/ja028839x.

(10) Sun, C.; Du, J.; Liu, J.; Yang, Y.; Ren, N.; Shen, W.; Xu, H.; Tang, Y. A Facile Route to Synthesize Endurable Mesopore Containing ZSM-5 Catalyst for Methanol to Propylene Reaction. *Chem. Commun.* **2010**, *46* (15), 2671. https://doi.org/10.1039/b925850g.

(11) Ravi, M.; Ranocchiari, M.; van Bokhoven, J. A. The Direct Catalytic Oxidation of Methane to Methanol—A Critical Assessment. *Angew. Chem. - Int. Ed.* **2017**, *56* (52), 16464–16483. https://doi.org/10.1002/anie.201702550.

(12) Barbaux, Y.; Elamrani, A. R.; Payen, E.; Gengembre, L.; Bonnelle, J. P.; Grzybowska, B. Silica Supported Molybdena Catalysts. Characterization and Methane Oxidation. *Appl. Catal.* **1988**, *44* (C), 117–132. https://doi.org/10.1016/S0166-9834(00)80048-2.

(13) Spencer, N. D. Partial Oxidation of Methane to Formaldehyde by Means of Molecular Oxygen. *J. Catal.* **1988**, *109* (1), 187–197. https://doi.org/10.1016/0021-9517(88)90197-2.

(14) Spencer, N. D.; Pereira, C. J. V2O5SiO2-Catalyzed Methane Partial Oxidation with Molecular Oxygen. *J. Catal.* **1989**, *116* (2), 399–406. https://doi.org/10.1016/0021-9517(89)90106-1.

(15) Barbero, J. A.; Alvarez, M. C.; Bañares, M. A.; Peña, M. A.; Fierro, J. L. G. Breakthrough in the Direct Conversion of Methane into C1-Oxygenates. *Chem. Commun.* **2002**, No. 11, 1184–1185. https://doi.org/10.1039/b202812n.

(16) Liu, H. F.; Liu, R. S.; Liew, K. Y.; Johnson, R. E.; Lunsford, J. H. Partial Oxidation of Methane by Nitrous Oxide over Molybdenum on Silica. *J. Am. Chem. Soc.* **1984**, *106* (15), 4117–4121. https://doi.org/10.1021/ja00327a009.

(17) Groothaert, M. H.; Smeets, P. J.; Sels, B. F.; Jacobs, P. A.; Schoonheydt, R. A. Selective Oxidation of Methane by the Bis(μ-Oxo)Dicopper Core Stabilized on ZSM-5 and Mordenite Zeolites. *J. Am. Chem. Soc.* **2005**, *127* (5), 1394–1395. https://doi.org/10.1021/ja047158u.

(18) Starokon, E. V; Parfenov, M. V; Pirutko, L. V; Abornev, S. I.; Panov, G. I. Room-Temperature Oxidation of Methane by R-Oxygen and Extraction of Products from the FeZSM-5 Surface. *J Phys Chem C* **2011**, *115*, 2155–2161. https://doi.org/10.1021/jp109906j.

(19) Vanelderen, P.; Hadt, R. G.; Smeets, P. J.; Solomon, E. I.; Schoonheydt, R. A.; Sels, B. F. Cu-ZSM-5: A Biomimetic Inorganic Model for Methane Oxidation. *J. Catal.* **2011**, *284* (2), 157–164. https://doi.org/10.1016/j.jcat.2011.10.009.

(20) Starokon, E. V.; Parfenov, M. V.; Pirutko, L. V.; Abornev, S. I.; Panov, G. I. Room-Temperature Oxidation of Methane by α-Oxygen and Extraction of Products from the FeZSM-5 Surface. *J. Phys. Chem. C* **2011**, *115* (5), 2155–2161. https://doi.org/10.1021/jp109906j.

(21) Hammond, C.; Forde, M. M.; Ab Rahim, M. H.; Thetford, A.; He, Q.; Jenkins, R. L.; Dimitratos, N.; Lopez-Sanchez, J. A.; Dummer, N. F.; Murphy, D. M.; Carley, A. F.; Taylor, S. H.; Willock, D. J.; Stangland, E. E.; Kang, J.; Hagen, H.; Kiely, C. J.; Hutchings, G. J. Direct Catalytic Conversion of Methane to Methanol in an Aqueous Medium by Using Copper-Promoted Fe-ZSM-5. *Angew. Chem. Int. Ed.* **2012**, *51* (21), 5129–5133. https://doi.org/10.1002/anie.201108706.

(22) Cicerone, R. J.; Oremland, R. S. Biogeochemical Aspects of Atmospheric Methane. *Glob. Biogeochem. Cycles* **1988**, *2* (4), 299–327. https://doi.org/10.1029/GB002i004p00299.

(23) Ab Rahim, M. H.; Forde, M. M.; Jenkins, R. L.; Hammond, C.; He, Q.; Dimitratos, N.; Lopez-Sanchez, J. A.; Carley, A. F.; Taylor, S. H.; Willock, D. J.; Murphy, D. M.; Kiely, C. J.; Hutchings, G. J. Oxidation of Methane to Methanol with Hydrogen Peroxide Using Supported Gold-Palladium Alloy Nanoparticles. *Angew. Chem. Int. Ed.* **2013**, *52* (4), 1280–1284. https://doi.org/10.1002/anie.201207717.

(24) Agarwal, N.; Freakley, S. J.; McVicker, R. U.; Althahban, S. M.; Dimitratos, N.; He, Q.; Morgan, D. J.; Jenkins, R. L.; Willock, D. J.; Taylor, S. H.; Kiely, C. J.; Hutchings, G. J. Aqueous Au-Pd Colloids Catalyze Selective CH4 Oxidation to CH3OH with O2 under Mild Conditions. *Science* **2017**, *358* (6360), 223–227. https://doi.org/10.1126/science.aan6515.

(25) Weaver, J. F.; Hakanoglu, C.; Hawkins, J. M.; Asthagiri, A. Molecular Adsorption of Small Alkanes on a PdO(101) Thin Film: Evidence of σ-Complex Formation. *J. Chem. Phys.* **2010**, *132* (2), 024709. https://doi.org/10.1063/1.3277672.

(26) Antony, A.; Hakanoglu, C.; Asthagiri, A.; Weaver, J. F. Dispersion-Corrected Density Functional Theory Calculations of the Molecular Binding of *n* -Alkanes on Pd(111) and PdO(101). *J. Chem. Phys.* **2012**, *136* (5), 054702. https://doi.org/10.1063/1.3679167.

(27) Antony, A.; Asthagiri, A.; Weaver, J. F. Pathways and Kinetics of Methane and Ethane C–H Bond Cleavage on PdO(101). *J. Chem. Phys.* **2013**, *139* (10), 104702. https://doi.org/10.1063/1.4819909.

(28) Sajith, P. K.; Staykov, A.; Yoshida, M.; Shiota, Y.; Yoshizawa, K. Theoretical Study of the Direct Conversion of Methane to Methanol Using $H_2O_2$ as an Oxidant on Pd and Au/Pd Surfaces. *J. Phys. Chem. C* **2020**, *124* (24), 13231–13239. https://doi.org/10.1021/acs.jpcc.0c03237.

(29) Freakley, S. J.; Agarwal, N.; McVicker, R. U.; Althahban, S.; Lewis, R. J.; Morgan, D. J.; Dimitratos, N.; Kiely, C. J.; Hutchings, G. J. Gold–Palladium Colloids as Catalysts for Hydrogen Peroxide Synthesis, Degradation and Methane Oxidation: Effect of the PVP Stabiliser. *Catal. Sci. Technol.* **2020**, *10* (17), 5935–5944. https://doi.org/10.1039/D0CY00915F.

(30) Kresse, G.; Hafner, J. *Ab Initio* Molecular Dynamics for Liquid Metals. *Phys. Rev. B* **1993**, *47* (1), 558–561. https://doi.org/10.1103/PhysRevB.47.558.

(31) Kresse, G.; Hafner, J. *Ab Initio* Molecular-Dynamics Simulation of the Liquid-Metal–Amorphous-Semiconductor Transition in Germanium. *Phys. Rev. B* **1994**, *49* (20), 14251–14269. https://doi.org/10.1103/PhysRevB.49.14251.
(32) Kresse, G.; Furthmüller, J. Efficiency of Ab-Initio Total Energy Calculations for Metals and Semiconductors Using a Plane-Wave Basis Set. *Comput. Mater. Sci.* **1996**, *6* (1), 15–50. https://doi.org/10.1016/0927-0256(96)00008-0.
(33) Kresse, G.; Furthmüller, J. Efficient Iterative Schemes for *Ab Initio* Total-Energy Calculations Using a Plane-Wave Basis Set. *Phys. Rev. B* **1996**, *54* (16), 11169–11186. https://doi.org/10.1103/PhysRevB.54.11169.
(34) Perdew, J. P.; Burke, K.; Ernzerhof, M. Generalized Gradient Approximation Made Simple. *Phys. Rev. Lett.* **1996**, *77* (18), 3865–3868. https://doi.org/10.1103/PhysRevLett.77.3865.
(35) Perdew, J. P.; Burke, K.; Ernzerhof, M. *ERRATA Generalized Gradient Approximation Made Simple [Phys. Rev. Lett. 77, 3865 (1996)]*; 1997.
(36) Blöchl, P. E. Projector Augmented-Wave Method. *Phys. Rev. B* **1994**, *50* (24), 17953–17979. https://doi.org/10.1103/PhysRevB.50.17953.
(37) Kresse, G.; Joubert, D. From Ultrasoft Pseudopotentials to the Projector Augmented-Wave Method. *Phys. Rev. B* **1999**, *59* (3), 1758–1775. https://doi.org/10.1103/PhysRevB.59.1758.
(38) Tereshchuk, P.; Da Silva, J. L. F. Ethanol and Water Adsorption on Close-Packed 3d, 4d, and 5d Transition-Metal Surfaces: A Density Functional Theory Investigation with van Der Waals Correction. *J. Phys. Chem. C* **2012**, *116* (46), 24695–24705. https://doi.org/10.1021/jp308870d.
(39) Tonigold, K.; Groß, A. Adsorption of Small Aromatic Molecules on the (111) Surfaces of Noble Metals: A Density Functional Theory Study with Semiempirical Corrections for Dispersion Effects. *J. Chem. Phys.* **2010**, *132* (22), 224701. https://doi.org/10.1063/1.3439691.
(40) Yu, Y.; Wang, X.; Lim, K. H. A DFT Study on the Adsorption of Formic Acid and Its Oxidized Intermediates on (100) Facets of Pt, Au, Monolayer and Decorated Pt@Au Surfaces. *Catal. Lett.* **2011**, *141* (12), 1872–1882. https://doi.org/10.1007/s10562-011-0719-7.
(41) Pozzo, M.; Alfè, D. Hydrogen Dissociation and Diffusion on Transition Metal (= Ti, Zr, V, Fe, Ru, Co, Rh, Ni, Pd, Cu, Ag)-Doped Mg(0001) Surfaces. *Int. J. Hydrog. Energy* **2009**, *34* (4), 1922–1930. https://doi.org/10.1016/j.ijhydene.2008.11.109.
(42) Monkhorst, H. J.; Pack, J. D. Special Points for Brillouin-Zone Integrations. *Phys. Rev. B* **1976**, *13* (12), 5188–5192. https://doi.org/10.1103/PhysRevB.13.5188.
(43) Grimme, S.; Antony, J.; Ehrlich, S.; Krieg, H. A Consistent and Accurate *Ab Initio* Parametrization of Density Functional Dispersion Correction (DFT-D) for the 94 Elements H-Pu. *J. Chem. Phys.* **2010**, *132* (15), 154104. https://doi.org/10.1063/1.3382344.
(44) Singh-Miller, N. E.; Marzari, N. Surface Energies, Work Functions, and Surface Relaxations of Low-Index Metallic Surfaces from FIrst Principles. *Phys. Rev. B* 9.
(45) Henkelman, G.; Uberuaga, B. P.; Jónsson, H. A Climbing Image Nudged Elastic Band Method for Finding Saddle Points and Minimum Energy Paths. *J. Chem. Phys.* **2000**, *113* (22), 9901–9904. https://doi.org/10.1063/1.1329672.
(46) Henkelman, G.; Jónsson, H. A Dimer Method for Finding Saddle Points on High Dimensional Potential Surfaces Using Only First Derivatives. *J. Chem. Phys.* **1999**, *111* (15), 7010–7022. https://doi.org/10.1063/1.480097.
(47) Bader, R. F. W.; Matta, C. F. Atoms in Molecules as Non-Overlapping, Bounded, Space-Filling Open Quantum Systems. *Found. Chem.* **2013**, *15* (3), 253–276. https://doi.org/10.1007/s10698-012-9153-1.
(48) Henkelman, G.; Arnaldsson, A.; Jónsson, H. A Fast and Robust Algorithm for Bader Decomposition of Charge Density. *Comput. Mater. Sci.* **2006**, *36* (3), 354–360. https://doi.org/10.1016/j.commatsci.2005.04.010.

(49) Tang, W.; Sanville, E.; Henkelman, G. A Grid-Based Bader Analysis Algorithm without Lattice Bias. *J. Phys. Condens. Matter* **2009**, *21* (8), 084204. https://doi.org/10.1088/0953-8984/21/8/084204.
(50) Yu, M.; Trinkle, D. R. Accurate and Efficient Algorithm for Bader Charge Integration. *J. Chem. Phys.* **2011**, *134* (6), 064111. https://doi.org/10.1063/1.3553716.
(51) Alvarez, S. A Cartography of the van Der Waals Territories. *Dalton Trans.* **2013**, *42* (24), 8617. https://doi.org/10.1039/c3dt50599e.
(52) Li, J.; Staykov, A.; Ishihara, T.; Yoshizawa, K. Theoretical Study of the Decomposition and Hydrogenation of $H_2O_2$ on Pd and Au@Pd Surfaces: Understanding toward High Selectivity of $H_2O_2$ Synthesis. *J. Phys. Chem. C* **2011**, *115* (15), 7392–7398. https://doi.org/10.1021/jp1070456.
(53) Blanksby, S. J.; Ellison, G. B. Bond Dissociation Energies of Organic Molecules. *Acc. Chem. Res.* **2003**, *36* (4), 255–263. https://doi.org/10.1021/ar020230d.
(54) Slater, J. C. Atomic Radii in Crystals. *J. Chem. Phys.* **1964**, *41* (10), 3199–3204. https://doi.org/10.1063/1.1725697.
(55) Plauck, A.; Stangland, E. E.; Dumesic, J. A.; Mavrikakis, M. Active Sites and Mechanisms for H2 O2 Decomposition over Pd Catalysts. *Proc. Natl. Acad. Sci. U. S. A.* **2016**, *113* (14), E1973–E1982. https://doi.org/10.1073/pnas.1602172113.
(56) Liu, X.; Conte, M.; Sankar, M.; He, Q.; Murphy, D. M.; Morgan, D.; Jenkins, R. L.; Knight, D.; Whiston, K.; Kiely, C. J.; Hutchings, G. J. Liquid Phase Oxidation of Cyclohexane Using Bimetallic Au–Pd/MgO Catalysts. *Appl. Catal. Gen.* **2015**, *504*, 373–380. https://doi.org/10.1016/J.APCATA.2015.02.034.